Recent Advances in Continuum Modeling of Interfacial and Transport Phenomena in Electric Double Layer Capacitors

Laurent Pilon,[*,z] Hainan Wang, and Anna d'Entremont

Henry Samueli School of Engineering and Applied Science Mechanical and Aerospace Engineering Department, University of California, Los Angeles, Los Angeles, California 90095, USA

This paper reviews recent advances in physical modeling of interfacial and transport phenomena in electric double layer capacitors (EDLCs) under both equilibrium and dynamic cycling. The models are based on continuum theory and account for (i) the Stern layer at the electrode/electrolyte interface, (ii) finite ion sizes, (iii) steric repulsions, (iv) asymmetric electrolytes featuring ions with different valencies, effective diameters, or diffusion coefficients, (v) electric-field-dependent dielectric permittivity of the electrolyte, and/or (vi) porous three-dimensional morphology of the electrodes. Typical characterization methods such as electrochemical impedance spectroscopy, cyclic voltammetry, and galvanostatic cycling were reproduced numerically to identify the dominant physical phenomena and to gain insight into experimental observations. In addition, recent thermal models derived from first principles for EDLCs under constant-current cycling accounting for irreversible Joule heating and reversible heat generation rates due to ion diffusion, steric effects, and changes in entropy are discussed. Scaling analyses of both equilibrium and dynamic models are also presented as a way to identify self-similar and asymptotic behaviors as well as to develop design rules for electrodes and electrolytes of next generation EDLCs. Throughout the document, special effort has been made to compare model predictions with experimental observations and reported data.

Electrical double layer capacitors (EDLCs) store energy by ion adsorption in the electrical double layer (EDL) forming at the electrode/electrolyte interfaces.[1,2] This process is highly reversible and the cycle life of EDLCs exceeds 100,000 cycles.[2,3] EDLCs can operate in a wide range of specific energy and power densities. This versatility is a key feature for electrical energy storage, energy harvesting, and energy regeneration applications.[2]

The performance of EDLCs is determined by the combination of the electrode material and morphology and of the electrolyte. In general, the key attributes of a good electrode include[1,3–7] (i) large surface area accessible to ions to maximize charge storage, (ii) optimum pore size, short pore length, and good pore connectivity to facilitate ion transport, (iii) large electrical conductivity to enable fast charging and discharging and low ohmic resistance, (iv) thin electrodes and current collectors to reduce the total resistance of the device, (v) small leakage current, (vi) small self-discharge, (vii) environmentally friendly materials, and (viii) low price. However, satisfying all these criteria simultaneously is challenging. For example, increasing surface area often results in larger electrode electrical resistivity.[1] Micropores with diameter less than 2 nm contribute greatly to EDLCs capacitance.[2] But pores smaller than the ion size are typically inactive and do not contribute to charge storage.[1,8] Porous electrodes must also be electrochemically accessible to ions. Then, interconnected mesopores with diameter ranging from 2 to 50 nm are necessary for fast charging thanks to their easier accessibility to ions.[1,6,9–11] In practice, electrodes of EDLCs are typically made of carbon-based materials including activated carbon,[12–16] carbon nanotubes,[16–28] templated carbons,[10,11,29,30] carbon aerogels,[31,32] and graphene.[33–35] Porous carbon materials are attractive for EDLC electrodes due to their easy processability, non-toxicity, high chemical stability, low density, large electrical conductivity, large surface area, and relatively low cost.[1,6,7]

The performance of EDLCs also strongly depends on the choice of electrolyte consisting of a salt dissolved in a solvent into its constituent ions. The ideal electrolyte solutions for EDLCs should feature[2]

(i) large ionic conductivity and mobility for fast charge-discharge rates, (ii) large dielectric constant, (iii) large chemical and electrochemical stability resulting in a large capacitance and long device lifetime, (iv) large temperature window to deliver power and energy at both low and high temperatures, as well as (v) low volatility, flammability, and toxicity for safety considerations. The choice of electrolyte strongly influences the effective electrical resistance of EDLCs. Two principal factors affect the electrical conductivity of the electrolytes (1) the concentration of the electrolyte and its ability to dissociate in cations and anions serving as free charge carriers and (2) the mobility of the dissociated ions in the electrolyte solution.[4] In addition, the operating voltage of EDLCs is determined by the electrochemical stability window of their electrolytes.[2,36] Above this critical voltage, electrolysis of the electrolyte occurs resulting in potential system failure and destruction. Both the energy and power densities of EDLCs depend quadratically on the maximum operating voltage. Thus, electrolytes with large electrochemical operational window are highly desirable.[2,36] Three main types of electrolytes have been used in EDLCs, namely aqueous electrolytes, organic electrolytes, and ionic liquids.[7,8] Two frequently used aqueous electrolytes are KOH and H_2SO_4 at high concentrations. Both have large electrical conductivity resulting in low device impedance and fast response time.[2] However, the maximum operating voltage for aqueous electrolyte solutions is typically restricted to about 1 V due to the electrochemical stability window of water (1.23 V).[2,4,37] This limits the energy density of EDLCs using aqueous electrolytes. Higher voltage can be achieved by using organic electrolytes which typically allow for voltages above 2 V.[4,37] Organic electrolytes used in commercial EDLCs generally consist of 1 M solutions of tetraethylammonium tetrafluoroborate TEABF$_4$ or triethylmethylammonium tetrafluoroborate TEMABF$_4$ in acetonitrile (AN) or propylene carbonate (PC).[2] However, the use of organic electrolytes is hindered by major limitations including their high cost, small electrical conductivity compared with aqueous electrolytes, low dielectric constant leading to smaller capacitance, complex purification procedures, as well as safety concerns due to their flammability and toxicity.[4] Finally, ionic liquids (ILs) are attractive candidates as electrolytes because of their high thermal stability, large decomposition voltage (>3 V), low

*Electrochemical Society Active Member.
zE-mail: pilon@seas.ucla.edu

volatility, non-flammability, and the variety of combinations of cations and anions available.[2,4,6] However, their relatively small electrical conductivity typically yields smaller power density than that achieved using organic electrolytes.[2,4,6]

To date, optimization of the porous morphology of electrodes and electrolytes used in EDLCs has been mainly carried out experimentally, by trial and error informed by physical intuition. However, the large number of variables to be considered and the different competing phenomena previously discussed make intuitive predictions difficult. In addition, experimental approaches are typically time consuming and costly. By contrast, rigorous physical modeling and accurate numerical tools could facilitate the design and optimization of the electrode morphology and the identification of the ideal electrolyte in a more systematic and efficient way. Physical modeling of supercapacitors is made difficult by the multiple and intimately coupled interfacial and transport phenomena simultaneously occurring in the device such as (i) charge transport in the electrodes, (ii) ion transport in the electrolyte and through the porous electrode structure driven by both electric field and concentration gradients, (iii) steric repulsion among ions, and (iv) local heat generation. Another challenge in modeling EDLCs is the multiscale nature of the system and the sometimes complex porous electrode morphology with unsolvated or solvated ions around 1 nm or less in diameter, pore size ranging from one to tens of nanometers, electrodes up to hundreds of microns thick, and devices several millimeters in size.

This paper aims to present recent advances in multiphysics and multiscale continuum modeling of interfacial and transport phenomena in EDLCs. The Background section introduces basic concepts and physical phenomena taking place in EDLCs. The Equilibrium Modeling section presents equilibrium models for EDLCs illustrated by detailed simulations of three-dimensional (3D) highly-ordered mesoporous carbon electrodes. This section also offers design rules for optimum EDLCs obtained from scaling analysis applied to experimental data for porous carbon electrodes with pores featuring a wide range of shapes and sizes. The Dynamic Modeling section and the Thermal Modeling section review dynamic models governing the spatiotemporal evolution of electric potential, ion concentrations, and temperature in EDLCs for different types of electrolytes. They present numerical simulations reproducing commonly used experimental characterization techniques such as electrochemical impedance spectroscopy (EIS), cyclic voltammetry (CV), and galvanostatic cycling. Finally, this review ends by discussing limitations of existing continuum models and providing recommendations for future research.

Background

Electrical double layer theories.— Figure 1 schematically shows different electrical double layer (EDL) models proposed over time. The concept of EDL was first introduced by Helmholtz[38] who suggested that a charged surface immersed in an electrolyte solution repels ions of the same charge (positive or negative) but attracts their counter-ions. The layer of electronic charge at the electrode surface and the layer of counter-ions in the electrolyte forms what has been termed the electrical double layer.[39,40] The Helmholtz model[38] hypothesized that counter-ions form a monolayer near the electrode surface, as illustrated in Figure 1a. This structure is analogous to that of conventional dielectric capacitors with two planar electrodes separated by a small distance H, approximated as the radius of an ion.[38-41]

The Helmholtz model was modified by Gouy[42] and Chapman[43] with the consideration that the ion distribution should be continuous in the electrolyte solution and given by the Boltzmann distribution. The Gouy-Chapman model accounts for the fact that the ions are mobile in the electrolyte solution under the combined effects of ion diffusion driven by concentration gradients and electromigration driven by the electric potential gradient, i.e., the electric field. This results in the so-called "diffuse layer" illustrated in Figure 1b. However, the Gouy-Chapman model overestimates the electrical double layer capacitance because it treats ions as point-charges resulting in unrealistically large ion concentrations at the electrode surfaces.[4,39,40]

In 1924, Stern proposed a new EDL model accounting for the finite size of ions. Stern[44] combined the Helmholtz model and the Gouy-Chapman model to explicitly describe two distinct regions, namely (1) the inner region of thickness H termed the Stern layer and (2) the outer region called the diffuse layer, as shown in Figure 1c. In the diffuse layer, the ions are mobile under the coupled influence of diffusion and electrostatic forces, and the Gouy-Chapman model applies in this layer.[36,39-41] In 1947, Grahame[45] improved this model by eliminating a number of deficiencies. The author emphasized that in the Stern layer, specific (covalent) and non-specific adsorption of ions at the same electrode surface lead to different closest distances from the charged surface.[4,36,40,41] The inner Helmholtz plane (IHP) consists of ions adsorbed by specific (covalent) forces and the outer Helmholtz plane (OHP), or Stern layer, of ion adsorbed by non-specific (electrostatic) forces. However, continuum models of EDLCs typically consider only electrostatic adsorption, corresponding to the Stern model. Note that electroneutrality does not prevail within the electrical double layer.[39,46-48]
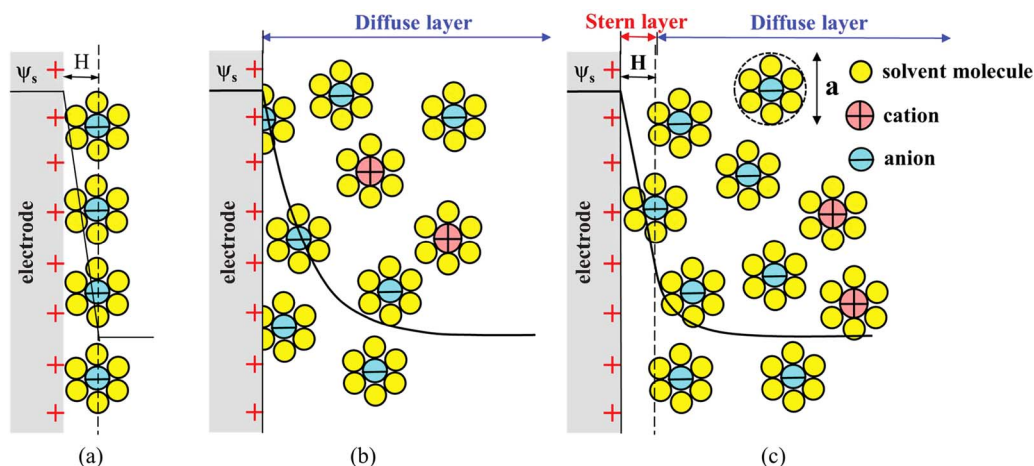

Figure 1. Schematic representation of electrical double layer structures according to (a) the Helmholtz model, (b) the Gouy-Chapman model, and (c) the Gouy-Chapman-Stern model. The double layer distance in the Helmholtz model and the Stern layer thickness are denoted by H while ψ_s is the potential at the electrode surface.

Electric double layer capacitors.— EDLC devices consist of two electrodes supported by their respective current collectors and separated by a separator impregnated with electrolyte. Each electrode is characterized by its capacitance defined per unit surface area, called the areal capacitance, and denoted by C_s (in F/m^2). Capacitance can also be defined per unit mass of electrode materials known as gravimetric capacitance and denoted by C_g (in F/g). The total capacitance C (in F) of an electrode is thus expressed as $C = C_s A_i = C_g m$ where A_i is the interfacial surface area between the electrode and the electrolyte, typically measured by gas adsorption porosimetry, and m is the mass of the electrode.

Furthermore, one can define the areal differential capacitance $C_{s,diff}$ and the areal integral capacitance $C_{s,int}$ of an electrode (both in F/m^2) respectively as,[36,41,49]

$$C_{s,diff} = \frac{dq_s}{d\psi_s} \quad \text{and} \quad C_{s,int} = \frac{q_s}{\psi_s} \qquad [1]$$

where q_s and ψ_s represent the electrode's surface charge density (in C/m^2) and its surface electric potential (in V) relative to the bulk electrolyte, respectively. Note that differential and integral capacitances can also be defined on a gravimetric basis. These definitions are independent of the experimental method used to measure them. However, note that capacitances measured using dynamic cycling methods may depend on the cycling period or frequency. In the limit of slow cycling, the capacitance becomes independent of the cycling rate and its value corresponds to the equilibrium capacitance.[50,51]

In the context of the the Gouy-Chapman-Stern model presented in Figure 1c, the differential, integral, and equilibrium areal capacitance of one electrode can be computed by considering the Stern and diffuse layer capacitances in series, i.e.,

$$\frac{1}{C_s} = \frac{1}{C_s^{St}} + \frac{1}{C_s^D} \qquad [2]$$

where C_s^{St} and C_s^D are respectively the Stern and diffuse layer areal capacitances on a differential, integral, or equilibrium basis.

An EDLC device with electrodes A and B can be treated as two capacitors in series with integral capacitances $C_A = C_{s,A} A_{i,A}$ and $C_B = C_{s,B} A_{i,B}$. Thus, the total integral capacitance C_T of the device is given by

$$\frac{1}{C_T} = \frac{1}{C_A} + \frac{1}{C_B}. \qquad [3]$$

Note that EDLC devices consisting of identical electrodes, such that $C_A = C_B$, have total capacitance $C_T = C_A/2$. Alternatively, for hybrid devices with a pseudocapacitive electrode, such that $C_B \gg C_A$, the total integral capacitance equals the smallest capacitance, i.e., $C_T = C_A$.

Finally, the total energy stored in the EDLC with electrodes A and B subjected to potential difference $\Delta\psi$ is typically approximated as $E = \frac{1}{2}C_{int,T}\Delta\psi^2$.[8,36,52] This suggests that in order to maximize the total EDLC energy storage, one needs to maximize the capacitance $C_{int,T}$ and the potential difference $\Delta\psi$ between the two electrodes. The total capacitance $C_{int,T}$ can be increased by increasing the surface area A_i of the porous electrodes. Note however that the areal capacitance $C_{s,int}$ depend on the porous structure of the two electrodes and on the accessibility of the electrode surface to ions. It may decrease as the total surface area of the electrodes increases.

RC circuit and homogeneous models.— Numerous equivalent RC circuit models[53–57] have been proposed and used to numerically investigate and predict the performance of EDLCs. They include but are not limited to (i) the simple series RC circuit, (ii) the so-called classical equivalent circuit[58] consisting of a resistor in parallel with a capacitor with an additional resistance in series, (iii) the three branch model with one voltage-dependent capacitance,[59] and (iv) the transmission line network model with an arbitrary number of equivalent RC circuit stages.[55,60,61] However, all these models suffer from several drawbacks.[62] First, they require prior knowledge of the resistance

and capacitance of the actual device which are typically determined experimentally.[58] Thus, this approach can be used for control but it cannot be used for designing and optimizing the electrode architecture and electrolyte of novel EDLCs. In fact, the above models successively add variables to better fit the experimental measurements. In addition, the concept of RC circuit models is inadequate for EDLCs since this approach inherently neglects ion diffusion and the time-dependent and non-uniform ion concentrations in the electrolyte.[63–65] Some intuitive arguments have been proposed to justify these RC circuit models. However, no rigorous justifications and validation have been provided. For example, the parallel resistance in the classical equivalent model was attributed to leakage current while the series resistance corresponded to the resistance of the electrolyte, the electrodes, and current collectors.[58] The transmission line network model was justified as a way to represent individual pores of the electrodes as a RC circuit connected in series.[60] However, the number of RC stages was typically small and not related to the electrode morphology.[55] Moreover, two different RC circuit models may produce the same impedance response. This suggests that fitted values of the resistances and capacitances in the RC circuit models provides "little or no direct information about the physical meaning of the elements for such models".[62] Finally, the fitted capacitance values based on complex RC circuits were also reported to underpredict those measured using other techniques.[66–70]

Alternatively, homogeneous models were also developed to investigate the charging / discharging dynamics of EDLCs. These models treat the heterogeneous microstructure of the electrodes as homogeneous with some effective macroscopic properties determined from effective medium approximations and depending on porosity and specific area.[71–82] However, these models imposed the specific area capacitance or the volumetric capacitance instead of predicting them. In addition, they cannot account for the detailed mesoporous electrode architecture.

Thermal considerations.— In applications such as energy storage onboard automobiles, EDLCs should be able to operate over a wide range of temperatures corresponding to various climates and seasons. Moreover, during EDLC charging and discharging, heat is generated internally, leading to temperature rise in the device. The heat generation rate depends on the cell's design, the electrode and electrolyte materials, and the operating conditions.[83] It has been established that increasing the EDLC temperature within a reasonable range significantly increases the EDLC performance.[84,85] This was attributed to the increase in electrolyte conductivity with increasing temperature.[84–87] However, EDLC operation at elevated temperatures may also result in (i) accelerated aging,[83,88–91] (ii) increased self-discharge rates,[88–90,92] (iii) increased cell pressure, and possibly (iv) electrolyte evaporation.[88] For example, a 10 K temperature rise or a 100 mV increase in cell voltage approximately doubles the aging rate.[91,92] EDLC aging results in permanent decrease in capacitance and increase in internal resistance leading, in turn, to larger heat generation rate and larger cell voltage.[55] In addition, temperature differences between cells in a series-connected EDLC module can cause voltage imbalances and destructive over-voltages of individual cells.[83,90] To avoid these harmful effects, temperature changes in EDLCs should be controlled.

This paper reviews recent efforts in physical modeling of interfacial and transport phenomena in EDLCs under either equilibrium or dynamic cycling conditions. Its aims to provide the interested reader with all the necessary information to perform multiscale and multiphysics simulations of EDLCs under realistic conditions. It systematically presents the governing equations, boundary conditions, and constitutive relationships to predict the local electric potential, ion concentrations, and/or temperatures based on continuum theory. All models discussed adopt the Gouy-Chapman-Stern model of EDLs presented in Figure 1c. Simulations based on actual experimental measurements were used to provide physical interpretations of experimental observations and design rules to achieve maximum energy storage performance. Similarly, several thermal models with different

levels of refinement are discussed as ways to predict operating temperatures and develop thermal management strategies for existing or novel EDLC designs. Comparison with experimental data reported in the literature is presented whenever possible.

Equilibrium Modeling

*Governing equations: modified Poisson-Boltzmann models.—Binary and symmetric electrolytes.—*For ideal electrolyte solutions with non-interacting ions treated as point charges, the electric potential is governed by the Poisson-Boltzmann (PB) equation.[93–99] The concentration profile of each ion species is given as a function of the local electric potential by the Boltzmann distribution. However, numerous studies have established that accounting for finite ion size is essential in order to accurately simulate electrical double layers for large electric potentials and/or large electrolyte concentrations typical of EDLCs.[93–107] Among the models accounting for the finite size of ions, the modified Poisson-Boltzmann (MPB) models are based on the local-density and mean-field approximations and are relatively convenient both mathematically and numerically.

Binary and symmetric electrolytes consist of two ion species (i = 1 or 2) with identical (i) effective ion diameter, i.e., $a_1 = a_2 = a$, (ii) opposite valency, i.e., $z_1 = -z_2 = z$ where z is a positive integer, and (iii) diffusion coefficient, i.e., $D_1 = D_2 = D$. Then, by virtue of electroneutrality, the bulk concentrations (in mol/L) of both ion species are identical, i.e., $c_{1,\infty} = c_{2,\infty} = c_\infty$. Among the different MPB models, Bikerman's model is the simplest for binary and symmetric electrolytes and is expressed as[95–104]

$$\nabla \cdot (\epsilon_0 \epsilon_r \nabla \psi)$$

$$= \begin{cases} 0 & \text{in the Stern layer} \quad [4a] \\[2em] \dfrac{2 z e N_A c_\infty \sinh\left(\frac{ze\psi}{k_B T}\right)}{1 + 4 N_A a^3 c_\infty \sinh^2\left(\frac{ze\psi}{2 k_B T}\right)} & \text{in the diffuse layer} \quad [4b] \end{cases}$$

where ϵ_0 and ϵ_r are the free space permittivity (ϵ_0 = 8.854 × 10^{-12} F/m) and the relative permittivity of the electrolyte solution, respectively. The Boltzmann constant is denoted by k_B = 1.38 × 10^{-23} J/K, e = 1.602 × 10^{-19} C is the elementary charge, N_A = 6.022 × 10^{23} mol^{-1} is the Avogadro number, while T is the temperature (in K). Note that under equilibrium conditions, there is no potential drop across the electrodes since there is no electric current. Therefore, the electric potential at the electrode/electrolyte interface is equal to that imposed at the current collectors. The local ion concentration $c_i(\mathbf{r})$ of ion species "i" at location $\mathbf{r}$ depends on the local potential $\psi(\mathbf{r})$, solution of Equation 4, and is expressed as[95,99]

$$c_i(\mathbf{r}) = \frac{c_\infty \exp\left(\frac{-z_i e \psi(\mathbf{r})}{k_B T}\right)}{1 + 4 N_A a^3 c_\infty \sinh^2\left(\frac{z_i e \psi(\mathbf{r})}{2 k_B T}\right)} \quad \text{for i = 1 and 2.} \quad [5]$$

Note that the concentration c_i of ions, treated as hard spheres of effective diameter a in the Bikerman model, cannot exceed the maximum concentration $c_{max} = 1/N_A a^3$ corresponding to simple cubic ion packing. This represents to a maximum ion volume fraction of $\pi/6 \approx 52\%$.

*Asymmetric electrolytes.—*Many electrolytes are asymmetric in nature due to the difference in (i) diffusion coefficient, (ii) size, and/or (iii) valency between their anions and cations, such as aqueous H_2SO_4 and Na_2SO_4. The recent literature reported MPB models valid for asymmetric electrolytes. For example, Borukhov et al.[108,109] and Silalahi et al.[110] developed MPB models valid for binary electrolytes with asymmetric valency but identical ion diameters. Their model was later extended to binary asymmetric electrolytes with unequal ion diameters.[111,112] Biesheuvel and co-workers[103,104,113] and Alijó et al.[114] developed more general MPB models valid for asymmetric electrolytes and/or multiple ion species with different ion sizes and valencies. This was accomplished by incorporating an excess

chemical potential term based on the Boublik-Mansoori-Carnahan-Starling-Leland equation-of-state. It directly relates the excess chemical potential to the local ion concentrations, ions' effective diameters, and their exclusion volumes.[103,104,113,114] In addition, Li and co-workers[107,115,116] developed a model for asymmetric electrolytes based on the variational principle while accounting for the finite sizes of both ions and solvent molecules. Alternatively, Horno and co-workers[102,117–122] developed a MPB model for asymmetric electrolytes by directly applying a Langmuir-type correction to the equilibrium ion concentration given by the Boltzmann distribution. By contrast, several studies have considered asymmetric electrolytes with different effective ion diameters by defining multiple Stern layers with different thicknesses near the electrode surface.[114,121–124] Only ion species of intermediate sizes existed in the intermediate Stern layer(s). However, the associated ion concentrations do not satisfy the overall electroneutrality condition across the electrolyte domain.[125] The different studies[104,105,107–109,115,116,123] have demonstrated that asymmetry in ion size and/or ion valency significantly affects the ion concentration and electric potential profiles near the electrode surface. However, to the best of our knowledge, these MPB models developed for asymmetric electrolytes have not been used to predict the capacitance of EDLCs.

*Boundary conditions.— Planar electrodes.—*Equations 4a and 4b are second order partial differential equations in terms of $\psi(\mathbf{r})$. Each requires two boundary conditions for each dimension of space in the Stern and diffuse layers, respectively. Figure 2 shows the schematic and the coordinate system for the reference case of an EDLC with two parallel planar electrodes at electric potentials ψ_s and $-\psi_s$ separated by a distance $2L$, with their respective Stern layers of thickness H. This case may seem trivial as it considers very simple geometry compared with actual porous electrode morphologies. However, such geometry facilitates the numerical simulations and enables one to understand the contributions and interactions among the different physical phenomena taking place simultaneously, as illustrated in the following sections.

For binary and symmetric electrolytes, the equilibrium potential $\psi(x)$ is antisymmetric. Thus, only half of the one-dimensional EDLC illustrated in Figure 2 may be simulated from the surface of one of the electrodes to the cell centerplane. Then, four boundary conditions are needed to solve Equation 4. They are given at the electrode/electrolyte interface ($x = L$), at the Stern/diffuse layer interface ($x = L - H$), and at the centerplane ($x = 0$) by[93]

$$\psi(L) = \psi_s \quad \text{and} \quad \psi(L - H^+) = \psi(L - H^-) \quad \text{in the Stern layer}$$
$$[6a]$$

$$\frac{\partial \psi}{\partial x}(L - H^+) = \frac{\partial \psi}{\partial x}(L - H^-) \quad \text{and} \quad \psi(0) = 0\,V \quad \text{in the diffuse layer}$$
$$[6b]$$

where ψ_s is the potential imposed at the electrode surface and H is the Stern layer thickness corresponding to half of the effective ion diameter a, i.e., $H = a/2$. It is important to note that the condition $\psi(x = 0) = 0$ V at the centerplane is not valid for asymmetric electrolytes.[125] Then, the entire electrolyte domain between the two electrodes needs to be simulated. Finally, extension of these boundary conditions to two-dimensional (2D) and three-dimensional (3D) geometries is straightforward.

Equation 4a indicates that the potential is linear in the Stern layer. Thus, the presence of the Stern layer can be accounted for via a different boundary condition to Equation 4b imposed at the Stern/diffuse layer interface located at $x = (L - H)$ and substituting Equations 6a and 6b by[95,99,126,127]

$$\frac{\partial \psi}{\partial x}(L - H) = \frac{\psi_s - \psi_D}{H} \quad \text{and} \quad \psi(0) = 0\,V \quad \text{in the diffuse layer}$$
$$[7]$$

where $\psi_D = \psi(L - H)$ is the potential at the Stern/diffuse layer interface computed numerically by solving Equation 4b. Then, one
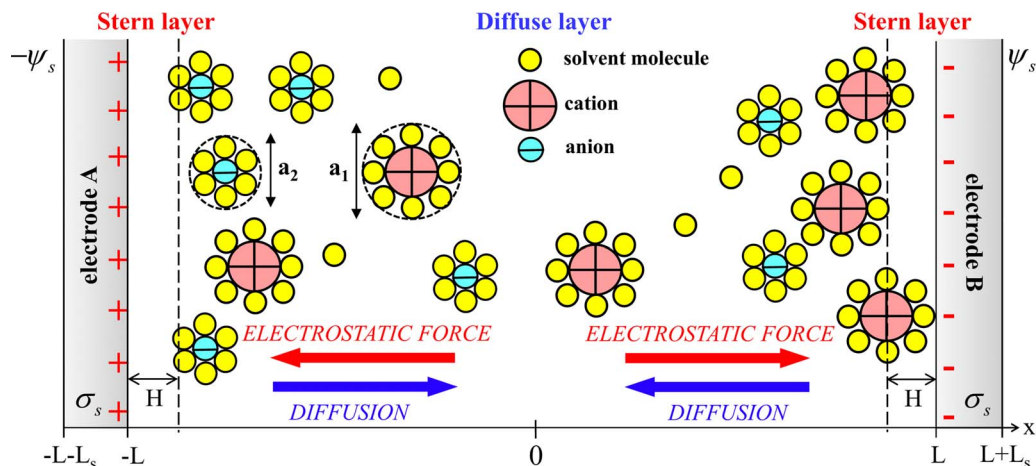
Figure 2. Schematic and coordinate system of an EDLC consisting of Stern and diffuse layers between two planar electrodes. Here, the ion diameters of large and small ion species were denoted by a_1 and a_2, respectively.

does not need to solve the MPB model and the associated boundary conditions in the Stern layer [Equations 4a and 6a].

Cylindrical or spherical electrode surface.—Wang and Pilon[128] extended Equation 7 to cylindrical and spherical electrodes or pores. For planar, cylindrical, and spherical electrodes illustrated in Figure 3a, the boundary conditions at the Stern/diffuse layer interface accounting for the presence of the Stern layer can be expressed as[128]

$$-\epsilon_0\epsilon_r(E_H)\nabla\psi\cdot\left(\frac{\mathbf{r}_H}{r_H}\right) = C_s^{St}\left(\frac{R_0}{R_0+H}\right)^p\left[\psi_s - \psi(\mathbf{r}_H)\right]. \quad [8]$$

Here, $\mathbf{r}_H$ is the local position vector of the Stern/diffuse layer interface located at $r_H = R_0 + H$ near the electrode surfaces. Here, the parameter p is such that (i) $p = 0$ for planar electrodes, (ii) $p = 1$ for cylindrical electrodes, and (iii) $p = 2$ for spherical electrodes of radius R_0.[128] In addition, $\epsilon_r(E_H)$ is the electrolyte relative permittivity evaluated at the Stern/diffuse layer interface based on the local electric field $E_H = E(\mathbf{r}_H)$ as discussed in the next section. Finally, C_s^{St} is the Stern layer capacitance predicted by the Helmholtz model and given by[93,128,129]

$$C_s^{St} = \begin{cases} \dfrac{\epsilon_0\epsilon_r(E_H)}{H} & \text{for planar electrodes,} \quad [9a] \\[2ex] \dfrac{\epsilon_0\epsilon_r(E_H)}{R_0\ln\left(1+\frac{H}{R_0}\right)} & \text{for cylindrical electrodes of radius } R_0, \\[1ex] & \hspace{4cm} [9b] \\[2ex] \dfrac{\epsilon_0\epsilon_r(E_H)}{H}\left(1+\dfrac{H}{R_0}\right) & \text{for spherical electrodes of radius } R_0. \quad [9c] \end{cases}$$

Moreover, for cylindrical and spherical pores of radius R_0 illustrated in Figure 3b, the boundary condition at the Stern/diffuse layer interface located at $r_H = R_0 - H$ can be written as[128]

$$-\epsilon_0\epsilon_r(E_H)\nabla\psi\cdot\left(\frac{\mathbf{r}_H}{r_H}\right) = C_s^{St}\left(\frac{R_0}{R_0-H}\right)^p\left[\psi_s - \psi(\mathbf{r}_H)\right]. \quad [10]$$

Here also, the Stern layer capacitance C_s^{St} for cylindrical ($p = 1$) or spherical ($p = 2$) pores is given by the Helmholtz model expressed as[129]

$$C_s^{St} = \begin{cases} \dfrac{\epsilon_0\epsilon_r(E_H)}{R_0\ln\left(\frac{R_0}{R_0-H}\right)} & \text{for cylindrical pores of radius } R_0, \\[1ex] & \hspace{4cm} [11a] \\[2ex] \dfrac{\epsilon_0\epsilon_r(E_H)}{H}\left(\dfrac{R_0-H}{R_0}\right) & \text{for spherical pores of radius } R_0. \\[1ex] & \hspace{4cm} [11b] \end{cases}$$

Note that when $R_0 \gg H$, Equations 8 and 10 reduce to Equation 7 for planar electrodes.

These alternative boundary conditions for planar, concave, and convex electrode surfaces were shown to accurately account for the Stern layer without explicitly simulating it in the numerical domain.[128]
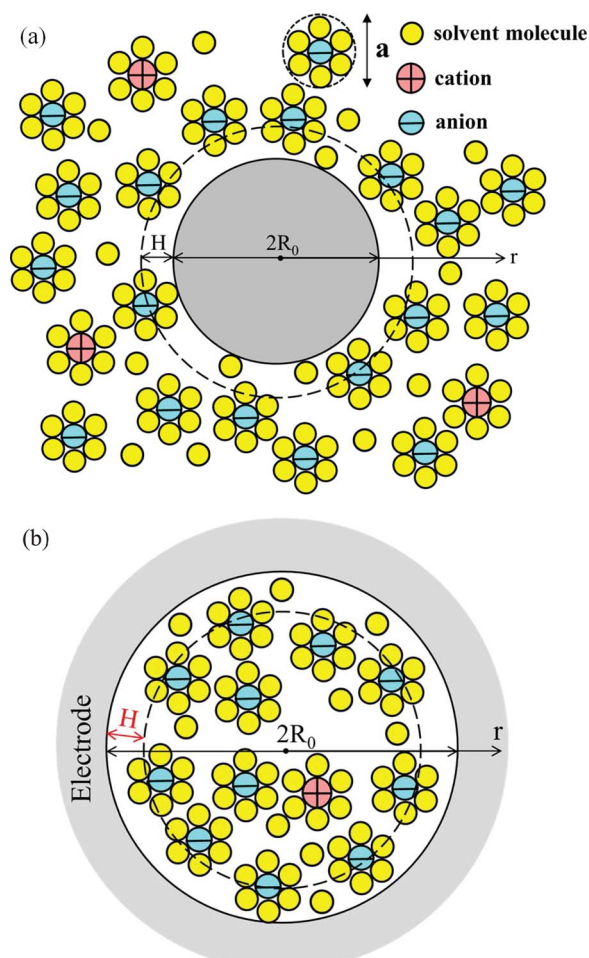

Figure 3. Schematic of the EDL structure forming near (a) a cylindrical or spherical electrode particle and (b) a cylindrical or spherical pore with radius R_0 and Stern layer thickness H and illustrating the arrangement of solvated anions and cations as well as the Stern layer and the diffuse layer.

Table I. Summary of Booth model parameters for commonly used aqueous and organic electrolyte solvents.

Solvent	$\epsilon_r(0)$	n	β (m/V)	Ref.
Water	78.5	1.33	1.41×10^{-8}	144, 145
PC	64.4	1.42	1.314×10^{-8}	146, 147
AN	35.97	1.34	3.015×10^{-8}	146, 148, 149

This presents the advantages of reducing the number of mesh elements used by the numerical method and thus the computational time. Such advantages become more significant with increasing electrode or pore radius and geometric complexity of the electrode architecture in general.

Constitutive relationships.— In order to solve the MPB model and the associated boundary conditions for the potential $\psi(\mathbf{r})$ in EDLCs under equilibrium conditions, several properties of the electrolyte are necessary including (i) the electrolyte relative permittivity ϵ_r, (ii) the ions' effective diameter a, and (iii) the ions' valency z. The relative permittivity ϵ_r of polar electrolytes has often been treated as constant and equal to that of the solvent at zero field.[94,97–99] However, the latter significantly decreases as the electric field increases to the large values typically encountered near the electrode surface of EDLCs.[130–132] In fact, the solvent dipole moments become highly oriented under large electric fields. Therefore, further orientation of the dipole moments can hardly provide more polarization leading to saturation and a decrease in the relative permittivity.[130–134] The Booth model accounts for the dependence of electrolyte solvent relative permittivity on the local electric field at large electric field.[130–132] It is expressed as

$$\epsilon_r(E)$$
$$= \begin{cases} n^2 + [\epsilon_r(0) - n^2]\frac{3}{\beta E}\left[\coth(\beta E) - \frac{1}{\beta E}\right] & \text{for } E \geq 10^7 \text{ V m}^{-1} \\ \epsilon_r(0) & \text{for } E < 10^7 \text{ V m}^{-1} \end{cases}$$

[12]

where $E = |-\nabla\psi|$ is the norm of the local electrical field vector, $\epsilon_r(0)$ is the solvent relative permittivity at zero electric field, and n is the index of refraction of the electrolyte at zero electric field frequency. Here, the coefficient β has units of m/V. Other models for $\epsilon_r(E)$ were reported in Ref. 133–143. Table I summarizes the values of $\epsilon_r(0)$, n, and β associated with the Booth model for common electrolyte solvents namely water, propylene carbonate (PC), and acetonitrile (AN).

Figure 4 plots the relative permittivity ϵ_r as a function of electric field for water, PC, and AN predicted by the Booth model with parameters listed in Table I along with predictions by molecular dynamics (MD) simulations for PC.[150] It indicates that the relative permittivity ϵ_r of AN is the smallest and decreases faster with increasing electric field E than those of water and PC. Moreover, simulations of spherical electrodes with radius less than 100 nm have established that the Stern and diffuse layers as well as the finite ion size and the field-dependent relative permittivity $\epsilon_r(E)$ of the electrolyte must be simultaneously accounted for in order to simulate accurately EDLCs under large surface electric potential and electrolyte concentrations such as those encountered in EDLCs featuring $\psi_s \approx 0.5$–1.5 V, $c_\infty \approx$ 1–6 M, and $E \approx 1$–5 V/nm.[93] For such conditions, ϵ_r is a fraction of its value at zero-electric field for these three electrolytes.

Moreover, the dielectric constant may be affected by polarization of the electrodes caused by the presence of ions in high concentration in the EDL and whose dielectric constant may differ from that of the solvent.[151] This effect can be accounted for via an additional chemical potential contribution based on the local effective dielectric constant expressed as a function of the ion volume fraction.[152]

Other input parameters to the equilibrium model include the ions' effective diameter a and their valencies z. Table II summarizes the properties of commonly used electrolytes such as KOH, H$_2$SO$_4$, NaCl, LiClO$_4$, and TEABF$_4$ in water, PC, and/or AN. The literature suggests
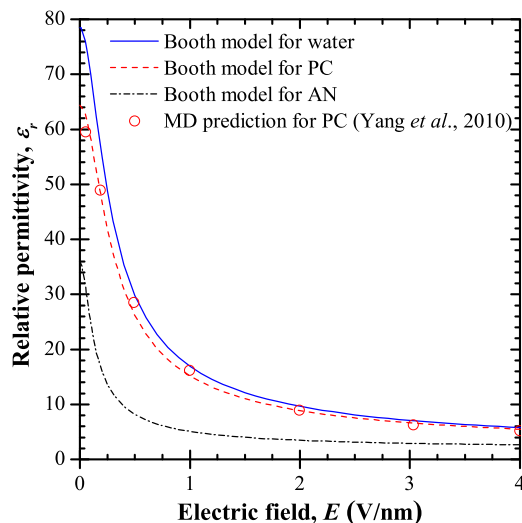

Figure 4. Comparison of the relative permittivity $\epsilon_r(E)$ of water, propylene carbonate (PC), and acetonitrile (AN) electrolyte as a function of electric field predicted by the Booth model [Eq. 12] using parameters summarized in Table I as well as predictions from MD simulations reported in Ref. 150 for PC.

that smaller bare ions tend to become more solvated resulting in larger solvated effective diameters.[95,99] Also, the solvated effective ion diameter tends to decrease with increasing concentration.[153,154]

Areal capacitances of planar electrodes.— Due to charge conservation, the total amount of charge Q_s in the electrode is equal to that present within the EDL. For planar electrodes, the electrode/electrolyte interfacial area A_s and the Stern/diffuse layer interfacial area A_d are equal so that $A_s = A_d$. However A_s and A_d are different for non-planar surfaces. In general, Q_s can be computed by integrating the surface charge density $q_s = \epsilon_0\epsilon_r\mathbf{E} \cdot \mathbf{n}$ over the surface A_s or A_d according to[39,163]

$$Q_s = \int_{A_s} \epsilon_0\epsilon_r(E)\mathbf{E} \cdot \mathbf{n}\, dA = \int_{A_d} \epsilon_0\epsilon_r(E)\mathbf{E} \cdot \mathbf{n}\, dA$$

[13]

where $\mathbf{E} = -\nabla\psi$ is the local electric field vector and $\mathbf{n}$ is the local outward normal unit vector at the surface considered. First, the equilibrium Stern layer capacitance $C_{s,eq}^{St}$ can be predicted from the Helmholtz model given by Equations 9 and 11 using the dielectric permittivity $\epsilon_r(E_H)$ estimated for the electric field vector $\mathbf{E}_H$ predicted at

Table II. Valency, non-solvated/solvated effective diameters a_i, and diffusion coefficient D_i of commonly used ions at 1 mol/L in aqueous and organic solvents.

Ions in electrolyte	z_i	a_i (nm)	D_i (m^2/s)	Ref.
H$^+$ in water	1	$-$/0.56	9.311×10^{-9}	154, 155
K$^+$ in water	1	0.266/0.66	1.957×10^{-9}	153, 154, 156
Na$^+$ in water	1	0.19/0.72	1.334×10^{-9}	153, 154
Li$^+$ in water	1	0.156/0.764	1.029×10^{-9}	155, 156
[TEA]$^+$ in water	1	0.80/0.80	0.868×10^{-9}	155, 156
OH$^-$ in water	-1	0.352/0.60	5.273×10^{-9}	153, 154
Cl$^-$ in water	-1	0.362/0.66	2.032×10^{-9}	153, 154
ClO$_4^-$ in water	-1	0.584/0.676	1.792×10^{-9}	155, 156
SO$_4^-$ in water	-2	0.58/0.758	1.065×10^{-9}	155, 156
Li$^+$ in PC	1	0.156/0.67	0.26×10^{-9}	156, 157
[TEA]$^+$ in PC	1	0.68/1.36	$-$	158–160
[BF$_4$]$^-$ in PC	-1	0.34/1.40	$-$	158–160
ClO$_4^-$ in PC	1	0.584/1.0	0.33×10^{-9}	156, 157, 161
[TEA]$^+$ in AN	1	0.68/1.304	0.96×10^{-9}	159, 162
[BF$_4$]$^-$ in AN	-1	0.34/1.156	0.82×10^{-9}	159, 162

the Stern/diffuse layer interface. Second, the diffuse layer areal equilibrium capacitance $C_{s,eq}^D$ and the total areal capacitance $C_{s,eq}$ can be respectively estimated as[146,164]

$$C_{s,eq}^D = \frac{Q_s}{\psi_D A_d} = \frac{1}{\psi_D A_d} \int_{A_s} \epsilon_0 \epsilon_r(E) \mathbf{E} \cdot \mathbf{n} \, dA \quad \text{and} \quad C_{s,eq} = \frac{Q_s}{\psi_s A_s}.$$
[14]

Here also, ψ_D denotes the potential at the Stern layer/diffuse layer interface. Note that $C_{s,eq}^{St}$, $C_{s,eq}^D$, and $C_{s,eq}$ satisfy Equation 2.

In the case of planar electrodes with binary and symmetric electrolytes with relative permittivity ϵ_r treated as constant, analytical expressions for the Stern and diffuse layers capacitances C_s^{St} and C_s^D can be obtained from the MPB model. They are given by[93,99,146]

$$C_{s,eq,planar}^{St} = \frac{\epsilon_0 \epsilon_r}{H} \quad \text{and}$$

[15]

$$C_{s,eq,planar}^D = \frac{2zeN_A c_\infty \lambda_D}{\psi_D} \sqrt{\frac{2}{\nu_p} \ln\left[1 + 2\nu_p \sinh^2\left(\frac{ze\psi_D}{2k_B T}\right)\right]}$$

where λ_D is the Debye length for binary and symmetric electrolytes defined as $\lambda_D = \sqrt{\epsilon_0 \epsilon_r k_B T / 2e^2 z^2 N_A c_\infty}$ and corresponding to an estimate of the EDL thickness.[39] The packing parameter ν_p is defined as $\nu_p = 2a^3 N_A c_\infty$.[95,99] It represents the ratio of the total bulk ion concentration $2c_\infty$ to the maximum ion concentration $c_{max} = 1/N_A a^3$ assuming a simple cubic ion packing and is always less than unity.[93,95,99,146] Then, combining Equations 2 and 15, the equilibrium areal capacitance for planar electrodes $C_{s,eq,planar}$ can be written as[146]

$$\frac{1}{C_{s,eq,planar}} = \frac{a}{2\epsilon_0 \epsilon_r} + \frac{\psi_D}{2zeN_A c_\infty \lambda_D}$$
$$\times \left\{\frac{2}{\nu_p} \ln\left[1 + 2\nu_p \sinh^2\left(\frac{ze\psi_D}{2k_B T}\right)\right]\right\}^{-1/2}.$$
[16]

Despite the convenient expression for $C_{s,eq,planar}^D$ given by Equation 15, the potential ψ_D remains unknown and needs to be determined by solving numerically the MPB model. Scaling analysis presented in Section Scaling Analysis will demonstrate that ψ_D is conveniently related to ψ_s by a power law.

Simulations of EDLCs with ordered porous electrodes.— Most continuum simulations of EDLCs have been limited to one-dimensional (1D) or quasi-two-dimensional electrode structures and/or have relied on fitting parameters.[146] To the best of our knowledge, Wang et al.[146] presented the first simulations of EDLCs with three-dimensional (3D) mesoporous electrodes consisting of highly-ordered and monodisperse mesoporous carbon spheres arranged in close packed structures. These simulations also accounted for the finite ion size as well as for the dependence of the electrolyte relative permittivity on the local electric field given by the Booth model [Equation 12] and were obtained using only properties reported in the literature. Due to the complex electrode morphology, the mesoporous structure was simplified by considering the areal capacitances of closely-packed non-porous carbon spheres and of a single mesopore inside a carbon matrix separately. Their Stern layer capacitance $C_{s,eq}^{St}$ was estimated from the Helmholtz model while the diffuse layer capacitance $C_{s,eq}^D$ was computed numerically by assuming $\psi_D = \psi_s$, i.e., by ignoring the Stern layer in the computational domain. The numerical predictions were in good agreement with the results reported by Liu et al.[165] for closely packed monodisperse mesoporous carbon spheres 250 nm in diameter with 10 nm mesopores for 1 M TEABF$_4$ in PC as the electrolyte. The results also indicated that the Stern layer capacitance and the field-dependent permittivity $\epsilon_r(E)$ need to be accounted in order to properly estimate the porous electrode capacitance.

To avoid this simplification and faithfully simulate the porous electrode morphology, Wang and Pilon[128] derived and used the jump boundary conditions given by Equations 8 and 10 along with the MPB model [Equation 4] to simulate 3D ordered bimodal mesoporous carbon electrodes. Figures 5a and 5b show SEM images of the bimodal porous carbon electrode synthesized by Woo et al.[166] with (a) highly ordered macropores and (b) mesoporous walls separating the large pores. Figures 5c and 5d show schematics and dimensions of the mesoporous structure simulated. The dimensions of the simulated electrode structure were identical to those of the bimodal mesoporous carbon CP204-S15 electrodes synthesized.[166] Figure 6 shows the measured gravimetric capacitance C_g (in F/g) of different bimodal carbon films[166] as a function of the specific surface area, ranging from 910 to 1030 m^2/g, obtained using 1 M TEABF$_4$ in PC. Figure 6 also shows the numerically predicted gravimetric capacitance as a function of specific surface area. The latter was varied by changing the macropore radius R_0 from 50 to 150 nm while other geometric parameters such as the carbon wall thickness and mesopore radius respectively remained 2 and 7 nm and identical to those of CP204-S15 mesoporous carbon.[166] The numerical results were obtained using either the solvated or the non-solvated effective ion diameters reported in the literature as $a = 1.40$ nm[159,160] or $a = 0.68$ nm,[158] respectively. It is evident that the predicted and experimentally measured gravimetric capacitances C_g increased linearly with increasing specific surface area. The predicted slope of C_g versus specific surface area corresponded to constant areal equilibrium capacitances of $C_s = 7.4$ or 10.2 μF/cm^2 when using solvated or non-solvated ion diameter, respectively.[128] This trend agreed very well with the experimental data reporting an areal capacitance of 9.4 F/cm^2.[166] These results also indicate that the choice of solvated versus non-solvated effective ion diameters makes a significant difference in the simulation results. Unfortunately, their values are not always reliably known.

Scaling analysis.— The previous section discussed equilibrium simulations accounting for the 3D porous structure of carbon electrodes. However, this type of simulations is limited to highly-ordered porous structures for which symmetry in the geometry and antisymmetry in the potential can be invoked to simplify the geometry and boundary conditions of the simulations. Unfortunately, many electrodes feature disordered, non-spherical, and/or polydisperse pores. At this time, such complex structures cannot be faithfully simulated numerically, even under equilibrium conditions, due to the computational cost required to simulate a representative elementary volume of the electrode. Alternatively, scaling analysis has been used by physicists and engineers to identify similarity behavior in complex systems. This section present how scaling analysis could be used to reduce the large number of design parameters of EDLCs to a few meaningful dimensionless numbers accounting for the dominant physical phenomena governing the behavior of the device. Then, engineering correlations can be derived relating the different dimensionless numbers identified using semi-empirical coefficients determined from a wide range of experimental data.

Planar electrodes.—Dimensional analysis of the MPB model for binary and symmetric electrolytes given by Equations 4a and 4b can be performed by scaling the spatial coordinate x by the Debye length λ_D and the local potential ψ by the thermal voltage $k_B T/ez$. The latter represents the voltage that would induce an electrical potential energy equivalent to the thermal energy of an ion of charge z. Then, the dimensionless variables are such that $x^* = x/\lambda_D$ and $\psi^* = \psi/(k_B T/ez)$.[167] Four dimensionless similarity parameters arise from the scaling analysis of the MPB model given by Equations 4 to 11, namely[167]

$$\psi_s^* = \frac{\psi_s}{(k_B T/ze)}, \quad \nu_p = \frac{c_\infty}{1/2N_A a^3}, \quad a^* = \frac{a}{\lambda_D}, \quad \text{and} \quad L^* = \frac{L}{\lambda_D} \quad [17]$$

where ψ_s^* is the dimensionless surface potential, ν_p is the packing parameter, a^* is the dimensionless ion diameter, and L^* is the dimensionless electrolyte layer thickness for planar electrodes. For cylindrical or spherical particles or pores, the spatial coordinate is r in cylindrical or spherical coordinates and the characteristic length scale is the average pore radius R_0. Then, x^* and L^* should be replaced by $r^* = r/\lambda_D$ and $R_0^* = R_0/\lambda_D$, respectively.
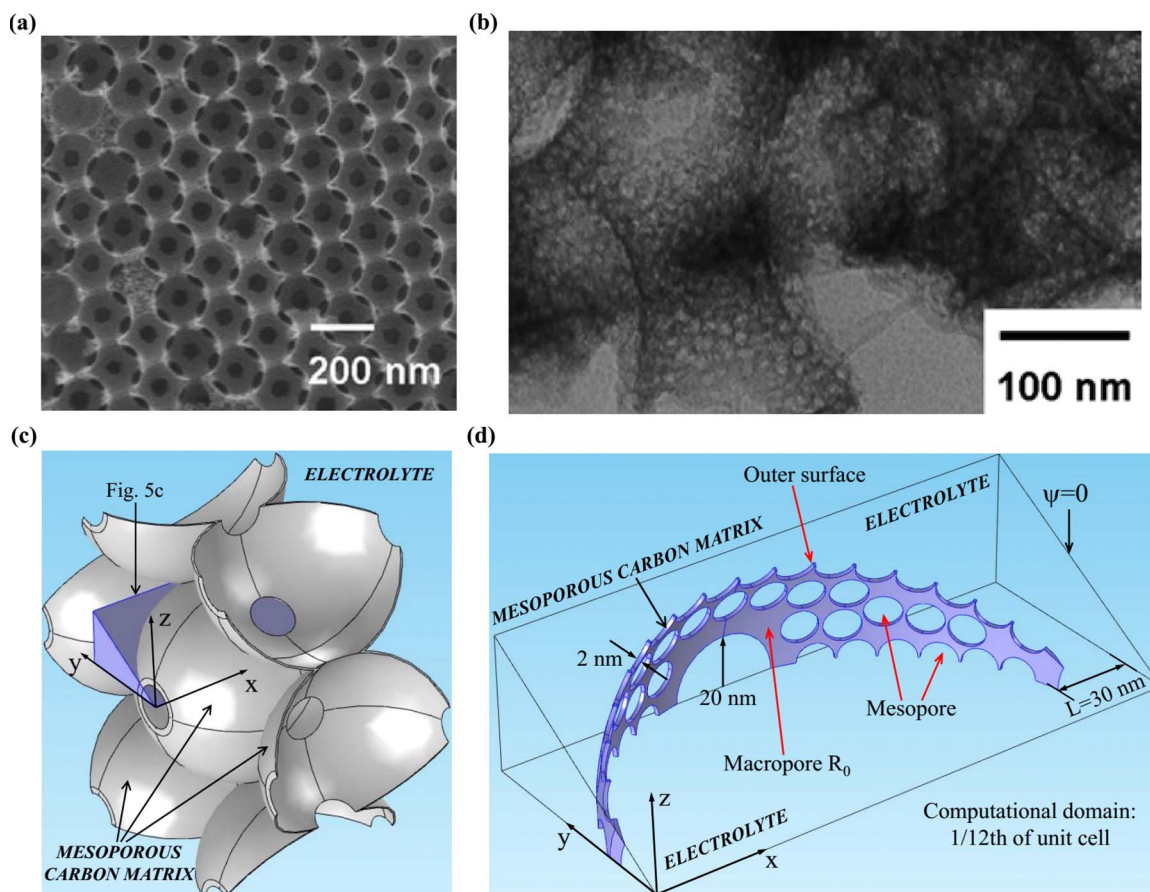
Figure 5. (a) FE-SEM images of 3D ordered bimodal porous carbon CP204-S15 and (b) TEM image of the mesoporous walls separating the large pores. Reproduced from Ref. 166 with permission of The Royal Society of Chemistry. (c-d) computational domain, coordinate system, and dimensions of the ordered bimodal mesoporous carbon simulated corresponding to CP204-S15.

Analytical expressions for the potential at the Stern/diffuse layer interface ψ_D, used in Equations 7 and 16, or ψ_D^* do not exist when accounting for the finite ion size, i.e., when $v_p \neq 0$. However, they can be determined numerically by solving the equilibrium MPB model with the Stern layer. For planar electrodes, a correla-

Figure 6. Predicted[128] and experimentally measured[166] gravimetric capacitance C_g for bimodal carbons as a function of their specific surface area. Numerical results were obtained by solving Equation 4 using boundary conditions given by Equations 8 and 10 with solvated or non-solvated ion diameters ($a = 1.40$ or 0.68 nm), $c_\infty = 1$ mol/L, $\psi_s = 2$ V, and the electrolyte permittivity $\epsilon_r(E)$ given by Equation 12. The specific surface area was adjusted by varying the inner macropore radius R_0 was varied from 50 to 150 nm.

tion was found[167] relating the dimensionless potentials ψ_D^* and ψ_s^* according to $\psi_D^* = 0.37\psi_s^{*1.16}$. This correlation was valid for a wide range of parameters, namely $0.01 \leq \psi_s^* \leq 20$, $16 \leq L^* \leq 329$, $0.052 \leq v_p \leq 0.94$, and $1.15 \leq a^* \leq 3.03$. It was also shown to apply to cylindrical or spherical pores with acceptable accuracy.[167] Then, a dimensionless equilibrium areal capacitance $C_{s,eq,planar}^*$ can be defined as $C_{s,eq,planar}^* = C_{s,eq,planar}/(2\epsilon_0\epsilon_r/a)$. Based on Equation 16, $C_{s,eq,planar}^*$ can be expressed in terms of the three dimensionless numbers identified previously ψ_s^*, v_p, and a^* as[167]

$$\frac{1}{C_{s,eq,planar}^*}$$
$$= 1 + \frac{0.74\psi_s^{*1.16}}{a^*}\left\{\frac{2}{v_p}\ln\left[1 + 2v_p\sinh^2\left(0.185\psi_s^{*1.16}\right)\right]\right\}^{-1/2} \quad [18]$$

This analytical expression can be conveniently used to predict the equilibrium areal capacitance of planar electrodes, assuming ϵ_r to be constant, without solving the MPB model.

Actual porous carbon electrodes.—In order to assess the applicability of the above scaling analysis to actual carbon-based porous electrodes, a wide range of experimental data was collected from the literature. They were selected to ensure that the electrolytes were binary and symmetric and the reported capacitance corresponded to the equilibrium areal capacitance.[167] Table III summarizes the experimental data reported in the literature for EDLCs with various electrolytes, electrode average pore radii R_0, and potential windows $\Delta\psi = 2\psi_s$, along with the corresponding range of the experimentally measured equilibrium areal capacitance, denoted by $C_{s,eq,exp}$ (μF/cm^2). The electrodes consisted of various micro and mesoporous carbons with average pore

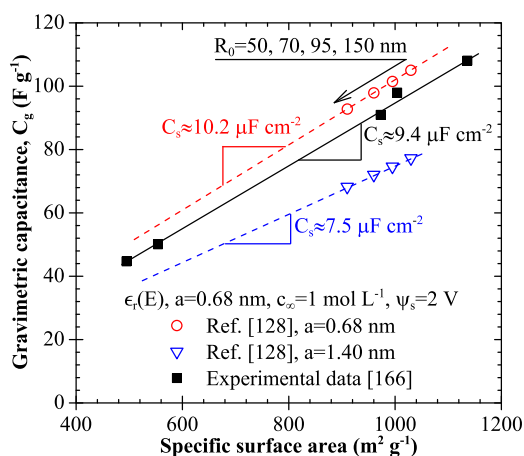**Table III. Summary of experimental data reported in the literature for various carbon electrodes, binary and symmetric electrolytes, potential window $\Delta\psi = 2\psi_s$, and average pore radius R_0 along with their integral areal capacitance $C_{s,eq,exp}$ (in μF/cm^2).**

Ref.	Electrode	R_0 (nm)	Electrolyte	$\psi_{max} - \psi_{min}$ (V)	$C_{s,eq,exp}$ (μF/cm^2)
158	TiC-CDC	0.68-1.09	1 M TEABF$_4$ in AN	2.3	6.0-13.6
168	OMC-M	2.15-4.25	6.88 M KOH	0.8	16.8-27.5
168	OMC-K	1.95-4.7	6.88 M KOH	0.8	12.0-22.5
169	GNS/CB	0.364-0.37	6 M KOH	1	28.3-46.6
170	HOMC	0.37-0.41	6 M KOH	1	8.2-11.2
171	FSMC	2.15	6 M KOH	0.6	19.4
172	OMC	1.35-3.0	6 M KOH	1	5.8-11.8
172	OMC	1.35-3.0	1 M TEABF$_4$ in AN	2	5.2-6.7
173	OMC	2.7-3.25	6.88 M KOH	0.89	11.9-15.0
174	CMK-8	2.39	2 M KOH	1	13.3
174	H-CMK-8	2.33	2 M KOH	1	20.2
175	OMC	2.25	6 M KOH	0.8	18.8
176	MC spheres	1.34	2 M KOH	1	11.1
177	MC	0.625-0.69	1 M TEABF$_4$ in AN	2	10.3-11.6
178	OMC	0.395-0.555	1 M TEABF$_4$ in PC	2	5.5-6.7
179	Carbon foam	1.9	6 M KOH	1	12.5
180	OMC	0.6	6 M KOH	0.8	14.1-19.6
181	GAC	0.245-0.26	6 M KOH	1	13.4-17.7
182	C-CS	1.95	6 M KOH	0.9	10.6-16

Note: solvent for KOH was water.

radii ranging from 0.36 to 3.25 nm. Three different electrolytes were considered and treated as binary and symmetric, namely aqueous KOH and TEABF$_4$ in PC or AN at concentrations c_∞ ranging between 1 and 6.88 mol/L. The effective diameters of anions and cations were assumed to be identical and equal to that of the smallest non-solvated ion.

Figure 7a plots a total of 56 experimental data points for the equilibrium areal capacitance $C_{s,eq,exp}$ as a function of the average pore radius R_0 for the experimental data summarized in Table III. The equilibrium areal capacitance varied between 5.5 and 47 μF/cm^2 due to the wide range of electrolytes, electrode morphologies, pore sizes, and potential windows considered. No obvious trend was apparent. Figure 7b shows the same data plotted in terms of the ratio $C_{s,eq,exp}/C_{s,eq,planar}$ as a function of $(R_0^* - a^*/2)$ where $C_{s,eq,planar}$ was predicted by Equation 18. The dimensionless numbers associated with the experimental data were such that $23 \leq \Delta\psi^* = 2\psi_s^* \leq 90$, $0.1 \leq \nu_p \leq 0.57$, $1.6 \leq a^* \leq 4.05$, and $1.4 \leq R_0^* \leq 40.2$. Figure 7b indicates that $C_{s,eq,exp}/C_{s,eq,planar}$ decreased from 0.5 to about 0.1 as $(R_0^* - a^*/2)$ increased from 0 to 40. First, it is remarkable that the experimentally measured equilibrium areal capacitances $C_{s,eq,exp}$ of such different mesoporous carbon electrodes had the same order of magnitude as the theoretical areal capacitance for planar electrodes $C_{s,eq,planar}$. In addition, plotting the data in terms of $C_{s,eq,exp}/C_{s,eq,planar}$ versus $(R_0^* - a^*/2)$ significantly reduced the scatter compared with Figure 7a. In fact, the dimensionless plot described a consistent trend. The capacitance ratio $C_{s,eq,exp}/C_{s,eq,planar}$ increased as the dimensionless pore radius R_0^* decreased and approached the dimensionless non-solvated ion radius $a^*/2$. On the other hand, the capacitance ratio $C_{s,eq,exp}/C_{s,eq,planar}$ reached a plateau around 0.08 as $R_0^* - a^*/2$ exceeded ~10. The scatter in the experimental data and the fact that $C_{s,eq,exp}$ differs from $C_{s,eq,planar}$ for large values of R_0 can be attributed to the following main reasons:[167] (i) The electrodes' pores feature a polydisperse size distribution whereas the scaling analysis used the average pore radius. (ii) The relative permittivity ϵ_r was assumed to be constant in the predictions of $C_{s,eq,planar}$. However, ϵ_r decreases significantly under the high electric fields encountered in actual EDLCs.[93,99,146] (iii) The electrolytes were assumed to be symmetric while actual anions and cations may have different ion diameters. And (iv) the assumption of simple cubic packing associated with the packing parameter ν_p used in the MPB model may be overly simplistic.

Overall, scaling analysis indicates that the equilibrium areal capacitance of mesoporous carbon electrodes with binary and symmetric
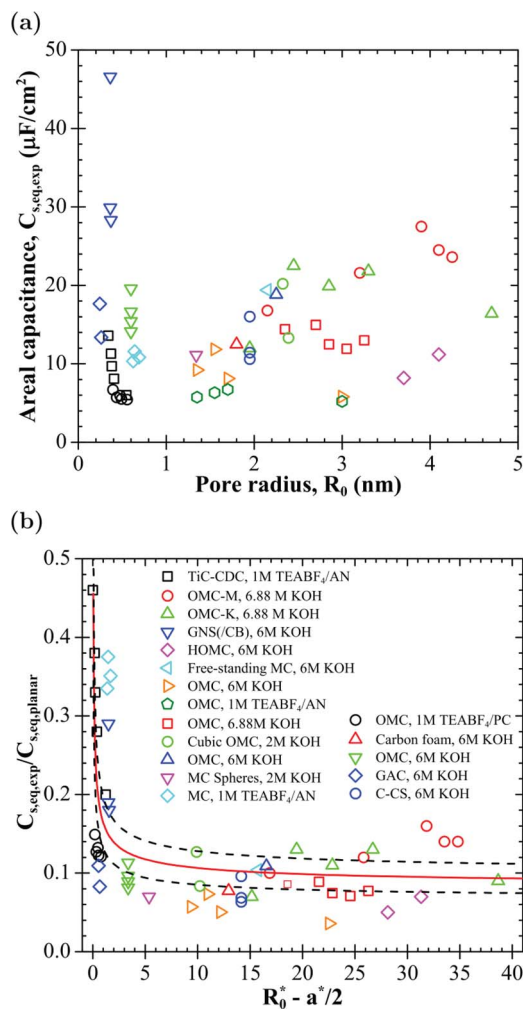

Figure 7. (a) Experimental data of equilibrium capacitance $C_{s,eq,exp}$ as a function of average pore radius R_0 and (b) the ratio $C_{s,eq,exp}/C_{s,eq,planar}$ as a function of $R_0^* - a^*/2$ for EDLCs with various mesoporous carbon electrodes and binary symmetric electrolytes. Reproduced with permission from Ref. 167.

electrolytes can be expressed as the product of the equilibrium areal capacitance of a planar electrode $C_{s,eq,planar}$ and a geometric function $f(R_0^* - a^*/2)$ correcting for the fact that pore/electrolyte interfaces are not planar, i.e.,[167]

$$C_{s,eq,pred} = C_{s,eq,planar} f(R_0^* - a^*/2). \qquad [19]$$

The geometric function $f(R_0^* - a^*/2)$ increased sharply as the pore radius approached the ion radius, i.e., $R_0 \approx (a/2)^+$ or $(R_0^* - a^*/2) \to 0^+$. On the other hand, it converged to a constant in the limiting case when pores were large compared with the ion radius, i.e., $R_0 \gg a/2$ or $(R_0^* - a^*/2) \gg 1$. Then, the effect of the pore curvature on the areal capacitance was negligible. Note also that the function $f(R_0^* - a^*/2)$ reached this constant value very rapidly for $(R_0^* - a^*/2)$ larger than 2-3. This suggests that electrode's pores should be as monodisperse as possible and their diameter should match those of the ions. Both of these criteria can be achieved with carbide-derived carbons which featured large capacitances.[158,183]

Dynamic Modeling

Modified Poisson-Nernst-Planck model.— Governing equations.— The modified Poisson Nernst-Planck (MPNP) model governs the spatiotemporal evolutions of the electric potential $\psi(\mathbf{r}, t)$ and ion concentrations $c_i(\mathbf{r}, t)$ in binary and symmetric electrolytes ($a_1 = a_2 = a$, $z_1 = -z_2 = z > 0$, and $D_1 = D_2 = D$) according to[64,95,184]

$$\nabla \cdot (\epsilon_0 \epsilon_r \nabla \psi) = \begin{cases} 0 & \text{in the Stern layer} \quad [20a] \\ -zeN_A(c_1 - c_2) & \text{in the diffuse layer} \quad [20b] \end{cases}$$

$$\text{with} \quad \frac{\partial c_i}{\partial t} = -\nabla \cdot \mathbf{N}_i \quad \text{in the diffuse layer, for } i = 1, 2. \quad [20c]$$

Here, $\mathbf{N}_i(\mathbf{r}, t)$ is the ion mass flux vector of ion species "i" (in mol/m^{2}s) at location $\mathbf{r}$ and time t defined as

$$\mathbf{N}_i(\mathbf{r}, t) = -D\nabla c_i - \frac{zFDc_i}{R_u T}\nabla\psi$$
$$- \frac{DN_A a^3 c_i}{1 - N_A a^3(c_1 + c_2)}\nabla(c_1 + c_2) \quad \text{for } i = 1, 2 \quad [21]$$

where $F = eN_A$ is the Faraday constant and D is the diffusion coefficient of both ion species. This model accounts for finite ion size and is applicable to cases with large electric potential and/or electrolyte concentrations. On the right-hand side of Equation 21, the three terms contributing to the ion mass flux $\mathbf{N}_i$ correspond to ion diffusion, electrostatic migration, and a correction due to the finite ion size, respectively.[95,99]

Finally, the electric potential within the electrodes is governed by the continuity equation combined with Ohm's law to give,[185,186]

$$\nabla \cdot (\sigma_s \nabla \psi) = 0 \qquad [22]$$

where σ_s is the electrical conductivity of the electrode material. Note that Equations 20 to 22 are coupled and thus must be solved simultaneously subject to proper initial and boundary conditions.

*Initial and boundary conditions.—*Zero electric potential and uniform ion concentrations equal to the bulk concentrations $c_{i,\infty}$ are typically used as initial conditions for solving the MPNP model in the electrolyte, i.e.,

$$\psi(x, t = 0) = 0\,V \quad \text{and} \quad c_i(x, t = 0) = c_{i,\infty}. \quad [23]$$

The boundary condition imposed at the current collector/electrode interface depends on the experiments simulated such as impedance spectroscopy (EIS), cyclic voltammetry (CV), or galvanostatic charging and discharging of EDLCs. For EIS measurements, the imposed electric potential can be expressed, in complex notation, as[41,187–189]

$$\psi_s(t) = \psi_{dc} + \psi_0 e^{i2\pi ft}. \qquad [24]$$

This harmonic potential consists of two components: (i) a time-independent "DC potential" ψ_{dc} and (ii) a periodically oscillating

potential with a small amplitude ψ_0 around the DC component.[189–191] The imaginary unit is denoted by i (i.e., $i^2 = -1$) while f is the frequency expressed in Hz.

In CV measurements, the potential at the current collector/electrode interface ψ_s varies periodically and linearly with time t according to,[125]

$$\psi_s(t) =$$
$$\begin{cases} \psi_{max} - v[t - 2(m-1)\tau_{CV}] & \text{for } 2(m-1)\tau_{CV} \le t < (2m-1)\tau_{CV} \\ & \qquad\qquad\qquad\qquad\qquad\quad [25a] \\ \psi_{min} + v[t - (2m-1)\tau_{CV}] & \text{for } (2m-1)\tau_{CV} \le t < 2m\tau_{CV} \\ & \qquad\qquad\qquad\qquad\qquad\quad [25b] \end{cases}$$

where v is the scan rate in V/s, $m(= 1, 2, 3, \ldots)$ is the cycle number, and $\tau_{CV} = (\psi_{max} - \psi_{min})/v$ is half the cycle period. The latter represents the time during which the surface potential varies from its maximum ψ_{max} to its minimum ψ_{min} value or vice versa. The difference $(\psi_{max} - \psi_{min})$ is the so-called "potential window". The corresponding boundary conditions in the 1D situation illustrated in Figure 2 for an EDLC devices made of planar electrodes are given by

$$\psi(-L - L_s, t) = -\psi_s(t) \quad \text{and} \quad \psi(L + L_s, t) = \psi_s(t). \quad [26]$$

Galvanostatic cycling consists of imposing a constant current density $\pm j_s$ at the electrode surface. Mathematically, the following 1D boundary condition is imposed at the electrode surface,[192]

$$-\sigma_s \frac{\partial\psi}{\partial x}(-L - L_s, t)$$
$$= \begin{cases} j_s & \text{for } (m-1)\tau_G \le t < \left(m - \frac{1}{2}\right)\tau_G \quad [27a] \\ -j_s & \text{for } \left(m - \frac{1}{2}\right)\tau_G \le t < m\tau_G \quad [27b] \end{cases}$$

where τ_G is the cycle period and $m = 1, 2, 3, \ldots$ is the cycle number. The opposite electrode surface may be grounded such that $\psi(L+L_s, t) = 0$ V. Note that this reference potential is arbitrary and affects neither the ion transport nor the resulting current and capacitances.[192]

Finally, in all cases, the electric potential and current density were continuous across the electrode/electrolyte interfaces at $x = \pm L$, i.e.,

$$\psi(\pm L^-, t) = \psi(\pm L^+, t) \quad \text{and}$$
$$\qquad\qquad\qquad\qquad\qquad\qquad\qquad\qquad [28]$$
$$-\sigma_s \frac{\partial\psi}{\partial x}(\pm L^-, t) = -\epsilon_0 \epsilon_r \frac{\partial^2\psi}{\partial x \partial t}(\pm L^+, t).$$

The boundary conditions accounting for the Stern layer used in equilibrium modeling and given by Equations 7 to 11 remain valid for the above transient characterization methods.[128] Finally, the ion mass flux vectors vanish at the Stern/diffuse layer interfaces located at $x = \pm(L - H)$ such that,[125]

$$\mathbf{N}_i(-L + H, t) = \mathbf{N}_i(L - H, t) = \mathbf{0} \qquad \text{for i = 1, 2.} \quad [29]$$

*Constitutive relationships.—*In addition to the constitutive relationships presented previously for equilibrium modeling, the diffusion coefficient D_i of each ion in the electrolyte and the electrical conductivity σ_s of the electrode materials are necessary in dynamic modeling of EDLCs. Table II summarizes the diffusion coefficient of various ions in commonly used electrolyte solutions. In addition, carbon is the material of choice for EDLC electrodes. Its electrical conductivity σ_s can vary from 10^{-6} to 10^2 S/m depending on its atomic structure.[193,194]

*Data processing.—*For the 1D device with planar electrodes shown in Figure 2, the current density $j_s(t)$ at the electrode/electrolyte interface located at $x = -L$ can be written as[125,195]

$$j_s(t) = -\epsilon_0 \epsilon_r \frac{\partial^2\psi}{\partial x \partial t}(-L, t). \qquad [30]$$

Electrochemical impedance spectroscopy (EIS) consists of imposing the potential $\psi_s(t)$ given by Equation 24. The resulting electric current $j_s(t)$ is measured and decomposed as

$$j_s(t) = j_{dc} + j_0 e^{i(2\pi ft - \phi)} \qquad [31]$$

where j_{dc} and j_0 are the DC current density and amplitude of the current density around its DC component, respectively; while $\phi(f)$ is the frequency-dependent phase angle between the harmonic potential $\psi_s(t)$ and the current density $j_s(t)$. The complex electrochemical impedance Z is defined as[41,187-189]

$$Z = \frac{\psi_0}{j_0} e^{i\phi} = Z' + i Z'' \qquad [32]$$

where Z' and Z'' (expressed in Ωm^2) are the real and imaginary parts of the impedance, respectively. Based on the equivalent series RC circuit, the resistance and differential capacitance per unit surface area are given by[41,87-89,96]

$$R = Z' \quad \text{and} \quad C_{s,diff}(f) = -\frac{1}{2\pi f Z''} \qquad [33]$$

where Z'' is the out-of-phase component of the measured impedance.[41,197] Note that EIS cannot measure the integral capacitance $C_{s,int}$.[198]

Alternatively, cyclic voltammetry (CV) consists of imposing a triangular potential $\psi_s(t)$ as a function of time [Equation 26] and measuring the resulting current density $j_s(t)$. The results are typically plotted in terms of current or current density j_s (in A/m²) versus electrode potential ψ_s, referred to as "CV curves". The surface charge density q_s accumulated at the electrode surface during one cycle can be estimated by computing the area enclosed by the CV curves. Then, the areal differential $C_{s,diff}$ and integral $C_{s,int}$ capacitances of one electrode are obtained as functions of the measured current density j_s at the scan rate $v = |d\psi_s/dt|$ (in V/s) according to,[198]

$$C_{s,diff}(v) = \frac{|j_s|}{v} \quad \text{and}$$

$$C_{s,int}(v) = \frac{q_s}{\psi_{max} - \psi_{min}} = \frac{1}{\psi_{max} - \psi_{min}} \oint \frac{j_s}{2v} d\psi_s. \qquad [34]$$

Note that at low scan rates, the areal integral capacitance is independent of scan rate and equal to the equilibrium capacitance of the electrode, i.e., $C_{s,int}(v \rightarrow 0) = C_{s,eq}$. Note that Equation 34 gives the expressions for the capacitances $C_{s,diff}$ and $C_{s,int}$ of one electrode and not those of the entire EDLC device.

The galvanostatic cycling method consists of charging and discharging the EDLC at constant current $\pm j_s$ [Equation 27] while measuring the cell or device potential $\psi_s(t)$. It can be used to measure both differential and integral capacitances according to,[198]

$$C_{s,diff}(j_s) = \frac{j_s}{|d\psi_s/dt|} \quad \text{and} \quad C_{s,int}(j_s) = \frac{j_s \tau_{G/2}}{\psi_{max} - \psi_{min}} \qquad [35]$$

where $\tau_{G/2}$ is the time required to vary the electric potential from ψ_{min} to ψ_{max} or vice versa under imposed current $\pm j_s$. The integral capacitance is more commonly reported than the differential capacitance for EDLCs tested using galvanostatic cycling method.[50,199-204] Note that in galvanostatic measurements, the areal capacitances $C_{s,diff}$ and $C_{s,int}$ calculated using Equations 35 are identical only when the measured electric potential varies strictly linearly with time. In fact, under very low electric potential ψ_s (for CV measurements) and low current j_s (for galvanostatic measurements), the surface charge density varies linearly with potential and $C_{s,diff} = C_{s,int}$.[99]

Sample simulations: physical interpretation of CV curves.—Wang and Pilon[195] performed 1D simulations of the two-electrode system illustrated in Figure 2 to provide physical interpretations of experimentally observed CV curves. Figure 8a shows the current density j_s versus surface potential ψ_s curves predicted from CV simulations for aqueous KCl electrolyte, treated as binary and symmetric, for three values
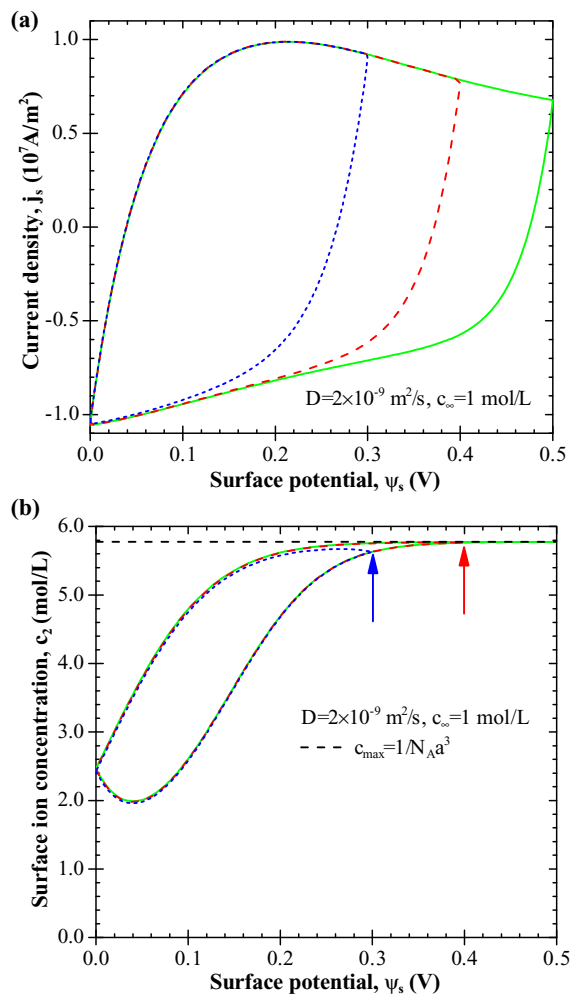

Figure 8. Predicted (a) j_s versus ψ_s and (b) $c_2(x = 0)$ versus ψ_s curves determined from CV simulations for three values of potential window, i.e., $\psi_{max} - \psi_{min} = 0.3, 0.4$, and 0.5 V. Results were obtained by numerically solving the MPNP model with a Stern layer without accounting for the electrode ($L_s = 0$ nm) for $v = 10^7$ V/s, $D = 2 \times 10^{-9}$ m²/s, $c_\infty = 1$ mol/L, and $L = 80$ nm.[195]

of potential window $\psi_{max} - \psi_{min} = 0.3, 0.4$, and 0.5 V. Results were obtained by solving the MPNP model with a Stern layer without accounting for the potential drop across the electrode, i.e., $\sigma_s \rightarrow \infty$. Other parameters were identical for all three cases and equal to $v = 10^7$ V/s, $a = 0.66$ nm, $D = 2 \times 10^{-9}$ m²/s, $c_\infty = 1$ mol/L, and $L = 80$ nm. Note that the scan rate was very large compared with experimental measurements because the simulations were performed for planar electrodes separated by a relatively thin electrolyte domain featuring small ionic resistivity.

First, it is worth noting that the numerically generated CV curves are very similar to those obtained experimentally with EDLCs for different potential windows.[205,206] Second, the three simulated CV curves reached a maximum current density at about $\psi_s = 0.2$ V during discharging while j_s decreased at larger surface potential. This hump is typical of experimental CV curves.[1,205,207-209] Different interpretations have been proposed in the literature to explain this hump including (i) electrolyte starvation due to limited amount of ions at low concentrations,[158,210] (ii) redox reactions at the electrode surface,[1,207-209,211-217] (iii) different ion mobilities between anions and cations,[215] and (iv) saturation of ions at the electrode surface.[205,206] However, there was no clear evidence and definitive explanation to the commonly observed hump in the CV curves.

To physically interpret the simulated CV curves, Figure 8b shows the surface anion Cl$^-$ concentration c_2 as a function of surface potential ψ_s for the same cases considered in Figure 8a. It also plots the maximum ion concentration $c_{max} = 1/N_A a^3$. It is evident that the surface anion concentration c_2 increased rapidly with increasing potential up to $\psi_s = 0.2$ V. This regime corresponded to the increase in current density j_s shown in Figure 8a due to the formation of an EDL of Cl$^-$ anions before their concentration reached its maximum at $\psi_s = 0.2$ V. For $\psi_s > 0.2$ V, the anion concentration asymptotically approached its maximum value c_{max}. In this regime, the ion accumulation near the electrode surface became slower as the electric potential increased due to steric repulsion resulting in decreasing current density j_s [Figure 8a]. Overall, these results demonstrate that the hump observed experimentally in CV curves for EDLCs can be attributed to the saturation of the electrode surface with closely packed ions as proposed in Ref. 205 and 206 based on experimental results. The hump does not appear to be caused by electrolyte starvation, redox reactions, or different ion mobility since these phenomena were not accounted for in the simulations.

Sample simulations: Galvanostatic cycling.—Simulations of galvanostatic cycling for binary and symmetric[192] or asymmetric[218] electrolytes and of EIS[198] can be found in the literature. These studies were also able to qualitatively reproduce experimental measurements and provide physical interpretation based on interfacial and transport phenomena. For example, Figure 9a shows the electric potential $\psi(x = -L, t)$ computed at the electrode surface located at $x = -L$ (Figure 2 as a function of time t.[192] The simulations were performed for electrolyte of thickness $L = 50$ μm at 298 K consisting of 1 M TEABF$_4$ in PC and treated as binary and symmetric with $z = 1$, $a = 0.68$ nm, $D = 1.7 \times 10^{-7}$ m^2/s, $c_\infty = 1$ M, and $\epsilon_r = 66.1$.[192] The EDLC was cycled at a constant current $j_s = 14$ mAcm^{-2} with a cycle period $t_c = 10$ ms. This current density was within the range of typical experimental values. The combination of j_s and t_c was chosen to yield a realistic maximum potential of 2.5 V for commercial EDLCs using organic electrolytes. However, the cycle period t_c was very small because the planar EDLC simulated charged very rapidly compared with actual porous electrodes. Figure 9a shows that the surface potential varied almost linearly between the minimum potential of 0 V and the maximum potential of 2.5 V and resembles typical galvanostatic cycling measurements on EDLCs. Figure 9b shows the corresponding concentration $c_2(x, t)$ of BF$_4^-$ anions as a function of location x at several times during a charging step near the same electrode. It indicates that surface ion concentration increased over time from initial concentration $c_\infty = 1$ M to $c_{max} = 1/N_A a^3 = 5.3$ M as the EDL formed. As charging proceeded, the closely packed ion layer at the electrode surface became thicker and the EDL region propagated inside the electrolyte domain. It is interesting to note that the ion concentration decreased from c_{max} to c_∞ over a very narrow spatial region featuring steep concentration gradients. This will result in significant local heat generation, as discussed in the Thermal Modeling section.

Generalized modified Poisson-Nernst-Planck model.— *Governing equations.*—The above MPNP model is valid only for binary and symmetric electrolytes. To overcome this limitation, Wang et al.[125] derived the so-called generalized MPNP (GMPNP) model from first principles based on excess chemical potential and Langmuir-type activity coefficient. It is valid for asymmetric electrolytes and/or in the presence of an arbitrary number N of ion species. The GMPNP model is expressed as[125]

$$\nabla \cdot (\epsilon_0 \epsilon_r \nabla \psi) = \begin{cases} 0 & \text{in the Stern layer} & [36a] \\ -e N_A \sum_{i=1}^{N} z_i c_i & \text{in the diffuse layer} & [36b] \end{cases}$$

$$\frac{\partial c_i}{\partial t} = -\nabla \cdot \mathbf{N}_i \quad \text{in the diffuse layer.} \qquad [36c]$$
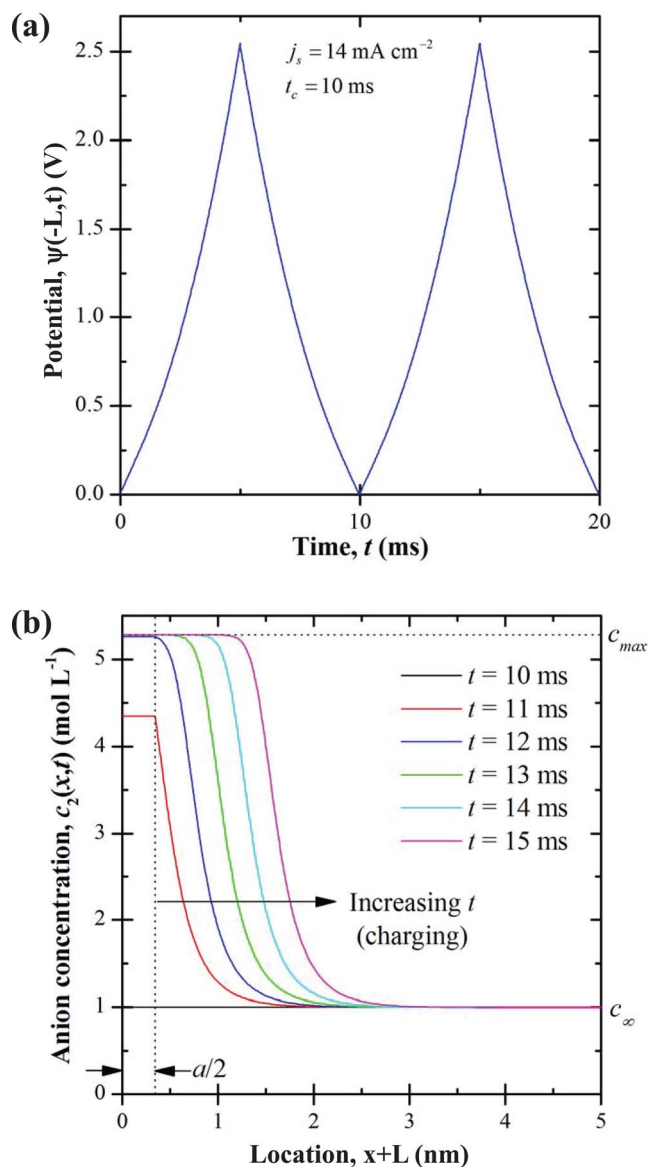

Figure 9. (a) Electric potential $\psi(-L, t)$ at the electrode surface at the Stern/diffuse layer interface as a function of time and (b) BF$_4^-$ anion concentration $c_2(x, t)$ as a function of location x at various times during galvanostatic cycles of period $t_c = 10$ ms and current density $j_s = 14$ mAcm^{-2}.[192]

Here, the general expression for mass flux vector $\mathbf{N}_i$ of ion species "i" is defined as

$$\mathbf{N}_i = -D_i \nabla c_i - D_i c_i \frac{z_i F}{R_u T} \nabla \psi - D_i c_i \frac{N_A \sum_{i=1}^{N} a_i^3 \nabla c_i}{1 - N_A \sum_{i=1}^{N} a_i^3 c_i}. \qquad [37]$$

For vanishing ion diameter ($a_i = 0$), the GMPNP model reduces to the classical PNP model.[95] In addition, for binary and symmetric electrolytes such that $N = 2$, $a_1 = a_2 = a$, $z_1 = -z_2 = z$, and $D_1 = D_2 = D$, the GMPNP model reduces to the MPNP model[99] presented in the Dynamic modeling section.

Here also, uniform ion concentrations and zero electric potential given by Equation 23 can be used as initial conditions. Note that electroneutrality in the electrolyte requires that $\sum_{i=1}^{N} z_i c_{i,\infty} = 0$. Unlike in binary and symmetric electrolytes, $c_{i,\infty}$ may differ from one species to another. The boundary conditions used in the MPNP model to

simulate EIS [Equation 24], CV [Equation 25], and galvanostatic cycling [Equation 27] and accounting for the Stern layer remain valid at all times for asymmetric electrolytes. The ion mass fluxes $\mathbf{N}_i$ still vanish at the Stern/diffuse layer interface [Equation 29]. Finally, constitutive relationships and properties used in the MPNP model can also be used for the GMPNP model. Note that the continuum models treat ion diffusion coefficient D_i, ion diameter a_i, and valency z_i as independent variables. In reality, ions with large effective diameter and/or valency have typically smaller diffusion coefficient,[153,154,156] as illustrated in Table II.

Scaling laws in CV measurements.— Dimensional analysis of the GMPNP model along with the boundary conditions reveal that CV simulations with binary and asymmetric electrolytes with planar electrodes were governed by twelve dimensionless similarity parameters expressed as[125]

$$v^* = \frac{\lambda_D^2/D_1}{(R_u T/z_1 F)/v}, \; \psi_{max}^* = \frac{\psi_{max}}{R_u T/z_1 F}, \; \psi_{min}^* = \frac{\psi_{min}}{R_u T/z_1 F}, \; L^* = \frac{L}{\lambda_D},$$

$$a_1^* = \frac{a_1}{\lambda_D}, \; a_2^* = \frac{a_2}{\lambda_D}, \; v_{p,1} = \frac{c_{1,\infty}}{1/2a_1^3 N_A}, \; v_{p,2} = \frac{c_{2,\infty}}{1/2a_2^3 N_A},$$

$$D_2^* = \frac{D_2}{D_1}, \; z_2^* = \frac{z_2}{z_1}, \; L_s^* = \frac{L_s}{\lambda_D}, \text{ and } \sigma_s^* = \frac{\sigma_s(\psi_{max}-\psi_{min})/L_s}{z_1 F c_{1,\infty} D_1/L}.$$

[38]

Here, v^* is the dimensionless scan rate. It can be interpreted as the ratio of the ion diffusion time scale ($\tau_{D_1} = \lambda_D^2/D_1$) to the characteristic time $\tau_{th} = (R_u T/z_1 F)/v$ for reaching the thermal potential $R_u T/z_1 F$ at scan rate v.[125] Here, the Debye length for asymmetric electrolytes with N ion species is expressed as $\lambda_D = (\epsilon_0 \epsilon_r R_u T/F^2 \sum_{i=1}^{N} z_i^2 c_{i,\infty})^{1/2}$.[39]

Moreover, ψ_{max}^* and ψ_{min}^* are the dimensionless maximum and minimum surface potentials, respectively, scaled by the thermal potential $R_u T/z_1 F$. They can also be interpreted as the ratio of characteristic times to reach ψ_{max} or ψ_{min} and the characteristic time τ_{th} at scan rate v.[125] Here, $v_{p,1}$ represents the packing parameter due to finite ion size of ion species "1". Note that v^*, ψ_{max}^*, ψ_{min}^*, L^*, a_1^*, and $v_{p,1}$ were identical to or direct combinations of the similarity parameters identified for the CV simulations of EDLCs with binary and symmetric electrolytes.[195] When considering binary and asymmetric electrolytes, three additional dimensionless numbers appear, namely $v_{p,2}$, D_2^*, and z_2^* associated with ion species 2 in addition to those obtained for binary and symmetric electrolytes. Accounting for the resistive losses through the electrode of thickness L_s and electrical conductivity σ_s results in dimensionless thickness $L_s^* = L_s/\lambda_D$ and electrical conductivity σ_s^* representing the ratio of the characteristic current density in the electrode $[\sigma_s(\psi_{max} - \psi_{min})/L_s]$ to that in the electrolyte $F z_1 c_{1\infty} D_1/L$.

Moreover, a dimensionless areal integral capacitance can be defined as

$$C_{s,int}^* = \frac{C_{s,int}}{z_1 e N_A D_1 c_{1,\infty}/\lambda_D v} = \frac{1}{\psi_{max}^* - \psi_{min}^*} \oint \frac{j_s^*}{2v^*} d\psi_s^* \quad [39]$$

where $C_{s,int}$ is defined by Equation 34. Graphically, $C_{s,int}^*$ corresponds to the area enclosed by the j_s^* versus ψ_s^* curve. The dimensionless capacitance $C_{s,int}^*$, for binary asymmetric electrolytes, depends on the twelve dimensionless numbers defined in Equation 38. However, finding a correlation such as that found for $C_{s,eq,planar}^*$ could be very challenging and time consuming. Instead, Wang et al.[125] identified a scaling law for EDLC integral capacitance in CV measurements with binary and asymmetric electrolytes between two planar electrodes. Figure 10a shows the double layer areal integral capacitance $C_{s,int}$ predicted from CV simulations as a function of scan rate v ranging from 10^{-2} to 10^8 V/s for cases with different dimensionless parameters L^*, z_2^*, ψ_{max}^*, ψ_{min}^*, D_2^*, a_1^*, a_2^*, v_{p1}, v_{p2}, σ_s^*, and L_s^*.[125] It is evident that the $C_{s,int}$ versus v curves differed significantly from one case to another due to the broad range of parameters considered. Figure
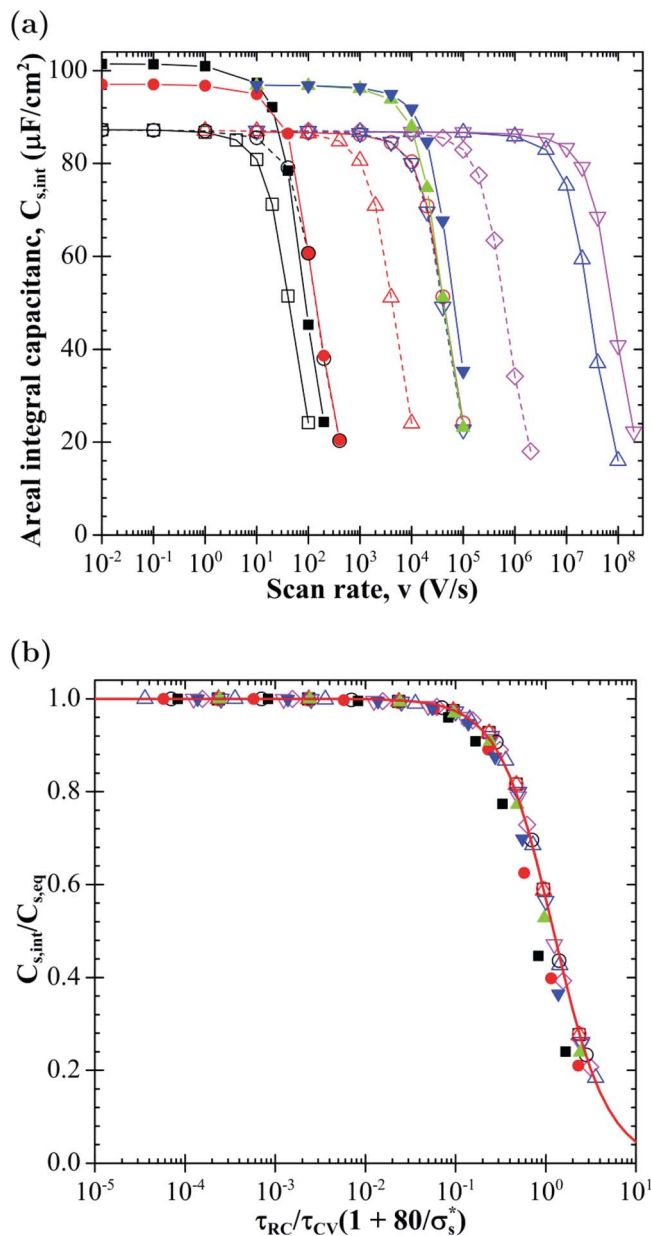

Figure 10. Predicted (a) capacitance $C_{s,int}$ as a function of scan rate v and (b) ratio $C_{s,int}/C_{s,eq}$ as a function of $(\tau_{RC}/\tau_{CV})(1 + 80/\sigma_s^*)$ obtained from CV simulations for different cases with various dimensionless parameters L^*, z_2^*, ψ_{max}^*, ψ_{min}^*, D_2^*, a_1^*, v_{p1}, v_{p2}, σ_s^*, and L_s^*.[125]

10b shows the same data as those shown in Figure 10a but plotted in terms of $C_{s,int}/C_{s,eq}$ as a function of $(\tau_{RC}/\tau_{CV})(1 + 80/\sigma_s^*)$ where $C_{s,eq}$ is the equilibrium capacitance corresponding to the maximum integral capacitance and the plateau observed in $C_{s,int}$ at low scan rates. Here, τ_{RC} is the "RC time scale" for binary and asymmetric electrolytes corresponding to the characteristic time of ions' electro-diffusion[63] and τ_{CV} is the half cycle period of CV measurements. They are expressed as,[125]

$$\tau_{RC} = \frac{\lambda_D L}{(D_1 + D_2)/2} = \sqrt{\tau_D \tau_L} \quad \text{and} \quad \tau_{CV} = \frac{\psi_{max} - \psi_{min}}{v} \quad [40]$$

where $\tau_D = 2\lambda_D^2/(D_1 + D_2)$ and $\tau_L = 2L^2/(D_1 + D_2)$ represent the characteristic times for ions to diffuse across the EDL and from one electrode to the other, respectively. The ratio τ_{RC}/τ_{CV} can also be

expressed in terms of the dimensionless numbers[125]

$$\frac{\tau_{RC}}{\tau_{CV}} = \frac{2v^*L^*}{(1+D_2^*)(\psi_{max}^* - \psi_{min}^*)} \quad [41]$$

First, it is remarkable that all the curves in Figure 10b collapsed on a master curve irrespective of the different values of the above dimensionless similarity parameters. Second, Figure 10b indicates that two regimes can be clearly identified:[125] (i) $\tau_{RC} \ll \tau_{CV}$ corresponds to the quasi-equilibrium or ion diffusion-independent regime and (ii) $\tau_{RC} \gg \tau_{CV}$ corresponds to the ion diffusion-limited regime. In the diffusion-independent regime, ion and charge transports are fast enough to follow the change in the surface potential $\psi_s(t)$, unlike in the diffusion-limited regime. Note that when σ_s^* is very large (e.g., $\sigma_s^* \gg 80$), the charge transport in the electrode is much faster than that in the electrolyte. Then, the potential drop across the electrode is negligible and it suffices to simulate the electrolyte to numerically generate CV curves.[125] This result also suggest that the electrode material should be such that $\sigma_s^* \gg 80$ for potential drop through the electrode to be negligible. Finally, note that this analysis is also valid in the limiting case of binary and symmetric electrolytes when $z_2^* = -1$, $a_2^* = a_1^*$, and $D_2^* = 1$, as considered in Refs. 63, 184, 195, and 219.

Thermal Modeling

Introduction.— Experimental studies of EDLCs have shown that galvanostatic cycling under current $\pm I_s$ (in A) caused an overall temperature rise from cycle to cycle as well as superimposed temperature oscillations with the same frequency as the charge-discharge cycles.[83,88,89,92,220–222] The overall temperature rise corresponded to irreversible Joule heating, while temperature oscillations were attributed to reversible heating.[92,220,221] Temperature measurements at the surface of a 5000 F commercial EDLC during galvanostatic cycling showed that the overall temperature rise in a thermally insulated EDLC was approximately linear and proportional to I_s^2.[92] The reversible heat generation rate within an EDLC was empirically found to be exothermic during charging, endothermic during discharging, and proportional to I_s.[92,221]

Thermal modeling of EDLCs aims to predict the temperature of EDLCs under specific operating conditions in order to avoid the negative effects associated with high temperature operation discussed earlier. In addition, detailed thermal models can be used to identify the different local interfacial and physical phenomena responsible for heat generation and to determine their respective contributions. Several fundamental questions are of particular interest: while Joule heating is well understood, what physical processes are responsible for reversible heat generation resulting in the experimentally-observed temperature oscillations? Also, does the reversible heat generation rate vary significantly with time and location within the EDLCs? These questions are addressed in the following sections.

Volume-averaged thermal modeling of EDLCs.— Volume-averaged thermal models of EDLCs assume that the temperature in the device is uniform and dependent only on time. Then, thermal energy balance performed on the entire EDLC yields the following governing equation for the volume-averaged device temperature $\bar{T}(t)$[92,223,224]

$$C_{th}\frac{d\bar{T}}{dt} = \dot{Q}(t) - \frac{(\bar{T} - T_\infty)}{R_{th}} \quad [42]$$

where C_{th} is the heat capacity of the device (in J/K) and $\dot{Q}(t)$ is the internal heat generation rate (in W). The term $(\bar{T} - T_\infty)/R_{th}$ represents the heat transfer rate (in W) from the device to its surroundings at temperature T_∞. The associated thermal resistance R_{th} (in K/W) can be expressed as $R_{th} = 1/\bar{h}A$, where $\bar{h}$ is the average convective heat transfer coefficient (in W/m²K) and A is the external surface area of the device (in m²). The total heat generation rate $\dot{Q}(t)$ consists of an irreversible and a reversible contribution, i.e., $\dot{Q}(t) = \dot{Q}_{irr}(t) + \dot{Q}_{rev}(t)$.

During galvanostatic cycling, the current is a square signal of magnitude I_s with cycle period t_c. Then, the irreversible heat generation rate is constant and equal to $\dot{Q}_{irr} = I_s^2R$, where R is the electrical equivalent series resistance of the EDLC.[92,221,225] Note, however, that most thermal models ignored $\dot{Q}_{rev}$ and determined R experimentally.[88,91,92,224] Schiffer et al.[92] developed an ad hoc model for the reversible heat generation rate $\dot{Q}_{rev}$ based on the fact that the entropy of the ions (i) decreased during charging as ions became more ordered due to EDL formation and (ii) increased during discharging as the ions returned to their disordered state corresponding to uniform ion concentrations.[92] These processes were respectively exothermic and endothermic to satisfy the second law of thermodynamics.[92] The derivation assumed that the EDL consisted of a monolayer of ions (Helmholtz model) and that the cell capacitance C_T was independent of the cell voltage. For a binary and monovalent electrolyte with symmetric ion size, the total reversible heat generation rate (in W) was expressed as[92]

$$\dot{Q}_{rev} = -2\frac{\bar{T}k_B}{e}\ln\left(\frac{V_S}{V_0}\right)C_T\frac{d\psi_s}{dt} = -2\frac{\bar{T}k_B}{e}\ln\left(\frac{V_S}{V_0}\right)I_s(t) \quad [43]$$

where V_0 and V_S are the total electrolyte volume and the Stern layer volume, respectively. The expression of $\dot{Q}_{rev}$ given by Equation 43 has been used in various studies.[91,222,224] Unfortunately, the volumes V_0 and V_S are difficult to evaluate for porous electrodes of commercial EDLCs. Instead, the value of $\ln(V_S/V_0)$ was used as a fitting parameter to match the model predictions with experimental data. A similar but simpler approach is to assume the reversible heat generation rate to be a square wave expressed as $\dot{Q}_{rev}(t) = +\alpha I_s$ during charging and $\dot{Q}_{rev}(t) = -\alpha I_s$ during discharging where α is a positive semiempirical parameter specific to each device (in V).[225]

Finally, the energy conservation Equation 42 is a first-order linear ordinary differential equation requiring only one initial condition often taken as room temperature, i.e., $\bar{T}(t = 0) = \bar{T}_0$. The temperature $\bar{T}(t)$ can be expressed as the sum $\bar{T}(t) = \bar{T}_{irr}(t) + \bar{T}_{rev}(t)$ where $\bar{T}_{irr}(t)$ and $\bar{T}_{rev}(t)$ correspond to the contributions of the irreversible and reversible heat generation rates to the temperature rise, respectively.[225] They are given by

$$\bar{T}_{irr}(t) = \bar{T}_0 + \left(I_s^2RR_{th} + T_\infty - \bar{T}_0\right)(1 - e^{-t/R_{th}C_{th}}) \quad \text{and} \quad [44]$$

$$\bar{T}_{rev}(t) = C_{th}^{-1}e^{-t/R_{th}C_{th}}\int_0^t e^{t'/R_{th}C_{th}}\dot{Q}_{rev}(t')dt'. \quad [45]$$

Temperature predictions obtained by solving Equation 42 showed good agreement with experimental data reported in the literature[92,88] for different commercial devices using C_{th}, R_{th}, R provided by the manufacturer while the parameter α was estimated as $\alpha = 2C_{th}\Delta\bar{T}_{rev}/I_st_c$ from the amplitude of the temperature oscillations $\Delta\bar{T}_{rev}$ measured experimentally under oscillatory steady-state conditions.[225]

Overall, the above volume-averaged model provides a rapid and easy way to predict the temperature of commercial EDLCs. It can be used to design appropriate thermal management strategies of individual or modules of EDLCs and to control charging and discharging for maximizing performance and minimizing aging.[91,224] Unfortunately, it cannot predict the thermal behavior of new EDLC designs without preliminary testing. More importantly, it cannot predict the spatiotemporal evolution of temperature within the device.

Local thermal modeling of EDLCs.— Local thermal models aim to predict the spatiotemporal evolution of the local temperature within the electrolyte, electrode, and current collector of an EDLC device. This can be achieved by solving the heat diffusion equation within the cell expressed as[223]

$$\rho c_p\frac{\partial T}{\partial t} = \nabla \cdot (k\nabla T) + \dot{q}. \quad [46]$$

Here ρ, c_p, and k are the density, specific heat, and thermal conductivity of the current collector, electrode, or electrolyte. In addition, $\dot{q}$

is the local volumetric heat generation rate (in W/m³).[223] It can be treated as uniform in the current collector and in the electrode and corresponds to irreversible Joule heating, i.e., $\dot{q} = j_s^2/\sigma_s$. In the electrolyte, the heat generation rate can be divided into irreversible and reversible contributions such that $\dot{q} = \dot{q}_{irr} + \dot{q}_{rev}$.

Equation 46 has been solved for two-dimensional[89,222] and three-dimensional cases.[220,226,227] Here also, most simulations considered the local temperature rise due only to irreversible heating but did not account for reversible heat generation.[89,90,220,226,227] The heat generation rate was prescribed as either (i) uniform throughout the entire device,[89,220,222,226,227] (ii) uniform in the "active components," i.e., the electrodes and separator,[226,227] or (iii) as having different values in the current collectors, electrodes, and separator.[90] Thermal models accounting for reversible heating[222] used the reversible heat generation rate in the electrolyte predicted by Schiffer et al.[92] assumed to be uniform, i.e., $\dot{q}_{rev} = \dot{Q}_{rev}/V$ where V is the electrolyte volume. Moreover, most of the local thermal models used experimental measurements to retrieve input parameters necessary to solve the model.[89,90,226,227] Local thermal models with uniform heat generation rates have shown good agreement with experimental temperature measurements for experimentally characterized EDLC devices.[89,222] However, they are semi-empirical models relying on experimentally measured device properties and ignoring the detailed electrochemical phenomena taking place during cycling. Thus, they are unable to predict (i) local variations in the heat generation rate, (ii) the performance of novel and untested EDLC designs, or (iii) how different device designs or materials would affect the thermal performance.

Recently, d'Entremont and Pilon[192,218] developed a local thermal model of EDLCs, from first principles, to predict the local irreversible and reversible heat generation rates based on the ion transport and on conservation of energy. The ion transport was modeled using (a) the MPNP model, presented in the Modified Poisson-Nernst-Planck model section, for binary and symmetric electrolytes[192] or (b) the GMPNP, discussed in the Generalized modified Poisson-Nernst-Planck model section, for asymmetric electrolytes.[218] The derivation of the energy conservation equation accounted for heat conduction and energy transport by ion mass fluxes.[192,218] The authors also obtained the well-known heat diffusion equation given by Equation 46 and rigorously derived an expression for $\dot{q}$ given by

$$\dot{q} = \dot{q}_E + \dot{q}_S = \dot{q}_{irr} + \dot{q}_{rev}. \qquad [47]$$

Here, $\dot{q}_E = \mathbf{j} \cdot \mathbf{E}$ is the heat generation associated with ions decreasing their electric potential[192,228,229] and $\dot{q}_S$ is the so-called "heat of mixing".[228,230] First, the irreversible volumetric heat generation rate, corresponding to Joule heating, was derived as one of three contributions to $\dot{q}_E$ and expressed as $\dot{q}_{irr} = j^2/\sigma_e$, where j is the local ionic current density (in A/m²) and σ_e is the local electrolyte conductivity (in S/m). For an electrolyte with N ion species "i" of valency z_i and concentration c_i, the current density $\mathbf{j}$ and the electrolyte conductivity σ_e can be expressed as,[48,231]

$$\mathbf{j} = \sum_{i=1}^{N} z_i F \mathbf{N}_i \qquad \text{and} \qquad \sigma_e = \frac{F^2}{R_u T} \sum_{i=1}^{N} z_i^2 D_i c_i(r, t) \qquad [48]$$

Second, the reversible heat generation rate $\dot{q}_{rev}$ arose in the EDL region due to the concentration and temperature gradients.[192,218] It was expressed as the sum of four different contributions,

$$\dot{q}_{rev} = \dot{q}_{E,d} + \dot{q}_{E,s} + \dot{q}_{S,c} + \dot{q}_{S,T} \qquad [49]$$

where $\dot{q}_{E,d}$ and $\dot{q}_{E,s}$ are contributions from $\dot{q}_E$ arising from ion diffusion and steric repulsion, respectively and such that $\dot{q}_E = \dot{q}_{irr} + \dot{q}_{E,d} + \dot{q}_{E,s}$. For asymmetric electrolytes with N ion species,

they were expressed as[218]

$$\dot{q}_{E,d} = \frac{\mathbf{j}}{\sigma_e} \cdot \left(F \sum_{i=1}^{N} D_i z_i \nabla c_i \right) \quad \text{and}$$

$$\dot{q}_{E,s} = \frac{\mathbf{j}}{\sigma_e} \cdot \frac{\left(F \sum_{i=1}^{N} D_i z_i c_i \right) \left(N_A \sum_{i=1}^{N} a_i^3 \nabla c_i \right)}{\left(1 - N_A \sum_{i=1}^{N} a_i^3 c_i \right)}. \qquad [50]$$

Note that $\dot{q}_{E,d}$ and $\dot{q}_{E,s}$ differ from zero only in the presence of an ion concentration gradient ∇c_i. On the other hand, the heat of mixing was such that $\dot{q}_S = \dot{q}_{S,c} + \dot{q}_{S,T}$ with the terms $\dot{q}_{S,c}$ and $\dot{q}_{S,T}$ arising from concentration gradients and from the temperature gradient, respectively. In the general case of asymmetric electrolytes, they were expressed as[218]

$$\dot{q}_{S,c} = \frac{3}{32\pi} \frac{eF^2}{(\epsilon_0 \epsilon_r)^{3/2} \left(R_u T \sum_{i=1}^{N} z_i^2 c_i \right)^{1/2}} \left(\sum_{i=1}^{N} z_i^2 \mathbf{N}_i \right) \cdot \left(\sum_{i=1}^{N} z_i^2 \nabla c_i \right)$$

$$\text{and} \quad \dot{q}_{S,T} = -\frac{3}{32\pi} \frac{eF^2 \left(\sum_{i=1}^{N} z_i^2 c_i \right)^{1/2}}{(\epsilon_0 \epsilon_r)^{3/2} R_u^{1/2} T^{3/2}} \sum_{i=1}^{N} z_i^2 \mathbf{N}_i \cdot \nabla T. \qquad [51]$$

Note that $\dot{q}_{S,T}$ was found to be negligible compared with $\dot{q}_{E,d}$, $\dot{q}_{E,s}$, and $\dot{q}_{S,c}$ for all cases simulated.[192,218] However, the latter three terms were of similar magnitude and particularly large near the electrode surface.

The numerical results indicated that $\dot{q}_{irr}$ was constant and uniform throughout the electrolyte for both symmetric[192] and asymmetric[218] electrolytes, as assumed in existing local models.[89,90,220,226,227] It decreased with increasing valency $|z_i|$ or diffusion coefficient D_i of one or both ion species due to the resulting increase in electrical conductivity σ_e of the electrolyte. By contrast, the reversible heat generation term $\dot{q}_{rev}$ was highly non-uniform, unlike what was assumed in the different implementations of Schiffer's model.[222] It was exothermic during charging, endothermic during discharging, and localized to a narrow region mainly in the EDL forming near the electrodes.[192,218] For symmetric electrolytes, $\dot{q}_{rev}$ was proportional to the current density j, as observed experimentally, and had the same magnitude but opposite signs near each electrode of the EDLC. However, in the general case of asymmetric electrolytes, $\dot{q}_{rev}$ was spatially asymmetric and, near a given electrode, was governed by the properties of the counterion. It increased with increasing valency $|z_i|$ and decreasing ion diameter a_i but was independent of diffusion coefficient D_i.

Figure 11 shows (a) experimental temperature measurements from a commercial EDLC with porous carbon electrodes under galvanostatic cycling[92] and (b) numerical temperature predictions at the centerline of an EDLC with planar electrodes illustrated in Figure 2 using $\dot{q}_{irr} = j^2/\sigma_e$ and $\dot{q}_{rev}$ given by Equations 49 to 51 for a binary and symmetric electrolyte.[192] The numerical predictions closely resembled those measured experimentally on the EDLC's casing.[192] Furthermore, predicted temperature oscillations near the electrode surface were larger and more angular than those at the centerline where $\dot{q}_{rev}$ was negligible[192] (not shown). The oscillations became smaller, smoother, and more delayed with increasing distance from the electrode surface as the reversible heat generated in the EDL was conducted to the rest of the electrolyte. These numerical results were also observed experimentally.[222] Therefore, temperature oscillations measured on the EDLC casing underestimate the internal temperature oscillations which can be very large near the electrode which may result in premature degradation of EDLC materials or electrolyte.

Finally, scaling analysis was also performed[232] for the local thermal model developed for binary and symmetric electrolytes.[192] It shows that reversible and irreversible heat generation rates were governed by seven dimensionless parameters that can be used to develop
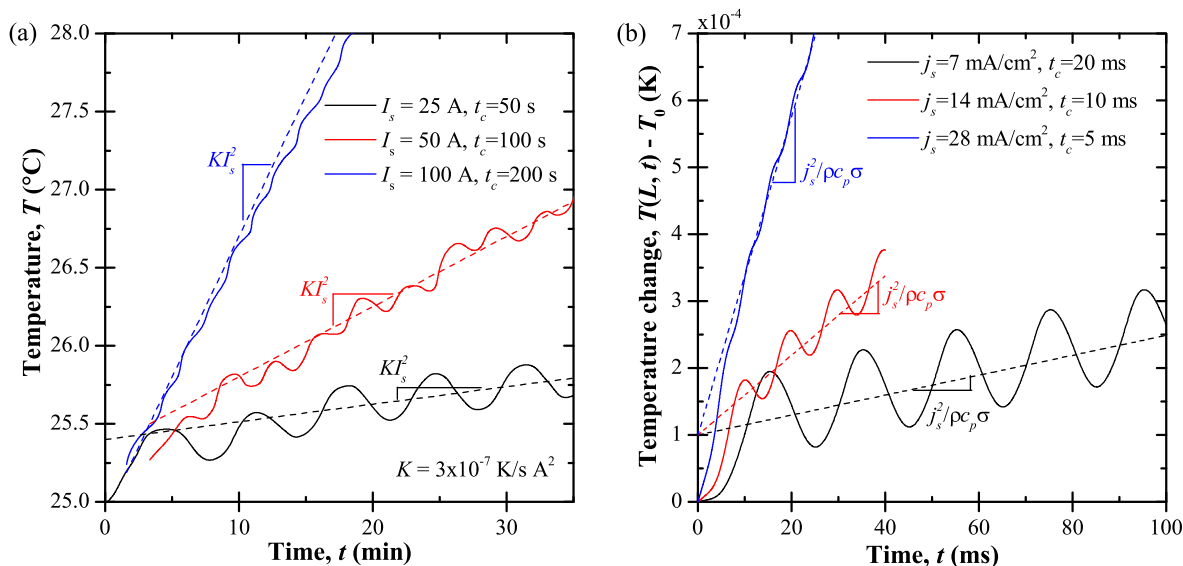
Figure 11. (a) Experimentally measured surface temperature of a thermally-insulated commercial EDLC during constant-current cycling at different currents over the potential window 1.5–2.5 V (Figure 1 0 from Ref. 92) and (b) numerically predicted temperatures at the centerline ($x = 0$) of a planar EDLC during constant-current cycling over the potential window 0–2.5 V.[192]

correlations for estimating heat generation in actual porous carbon electrodes.

Overall, local thermal models derived from first principles qualitatively predicted the experimentally observed thermal behavior of EDLCs. The rigorous theoretical derivation offers insight into the physical causes of EDLC heating and its detailed spatial and temporal evolution. In practice, to reduce heat generation in EDLCs, electrolytes should feature large bulk concentrations $c_{i,\infty}$ and at least one ion species with large diffusion coefficient to achieve large electrical conductivity. In addition, electrolytes chosen to yield large capacitance via ions with large valency $|z_i|$ and/or small diameter a_i are likely to feature large reversible heat generation rates generated near the electrode surfaces.

Conclusions and Prospects

Significant progress has been made in physics-based continuum modeling of EDLCs under both equilibrium and dynamic conditions. To accurately simulate actual EDLCs, the models should simultaneously account for (i) both Stern and diffuse layers, (ii) finite ion size, (iii) the dependence of electrolyte permittivity on the local electric field, (iv) the asymmetric nature of the electrolyte (if applicable), and (v) the curvature of the electrode surface.[93,146]

The equilibrium capacitance of highly-ordered mesoporous electrodes can be predicted by using the modified Poisson-Boltzmann model. This has been facilitated by the development of new boundary conditions accounting for the presence of the Stern layer without resolving it in the computational domain.[128] Alternatively, scaling analysis was applied to experimentally measured integral capacitance of mesoporous carbon electrodes with a wide range of morphology and different electrolytes. Then, scaling laws governing the performances of actual EDLCs with various porous architectures were developed to rationalize the design of EDLCs and provide rules for optimizing the porous architecture of EDLCs and for selecting the electrolyte. This led to the following design rules to maximize the integral areal capacitance (i) the effective ion diameter a should be small, (ii) the electrolyte dielectric constant ϵ_r should be large, (iii) the pores should be monodisperse and their radius R_0 tailored to match the ion diameter, i.e., $2R_0 \approx a$, and (iv) the ion valency z should be large.

The charging/discharging dynamics of EDLCs can be modeled using the MPNP model for binary and symmetric electrolytes and the GMPNP model for asymmetric electrolytes.[125,195] Similarly, a lo-

cal transient thermal model rigorously derived from first principles was presented. It provides expressions of the local reversible and irreversible heat generation rates. Detailed transient simulations of the various interfacial and transport phenomena taking place in EDLCs have enabled rigorous physical interpretation of experimental observations from cyclic voltammetry and galvanostatic cycling. Finally, scaling analysis of the different dynamic models have illustrated self-similar behaviors and identified meaningful dimensionless parameters governing the charging and discharging performance of EDLCs as well as heat generation therein.

Important future work in modeling of EDLCs includes simulating the charging/discharging dynamics of EDLCs featuring three-dimensional porous electrodes with realistic length scales and accounting for potential drops within the electrode materials or a 3D scaffold structure and across interfaces. This could offer a direct way to identify key design parameters of the electrode architecture for improving the energy and power densities of actual EDLC electrodes and devices. However, this effort would require significant computational resources. Alternatively, volume-averaging theory[233] could be applied to the above equations averaged over a representative elementary volume (REV) to account for macroscopic morphological parameters of the porous electrodes such as porosity, interfacial surface area, and effective transport properties. Moreover, the GMPNP models previously developed for an arbitrary number of ion species could be used to investigate mixtures of two or more electrolytes as a way of extending the working conditions and performances of EDLCs.[234] It is unclear how several anions or cations with different diameters, valencies, and diffusion coefficients would interact near the electrode surface. Moreover, simulations could address the following questions: in a bimodal or polydisperse mesoporous electrode, would the small and large ions accumulate differently at the electrode/electrolyte interface? Is an ordered porous structure more beneficial for ion transport and EDL formation than a disordered one? What would be the optimum morphology and dimensions of the porous electrode structure?

MD simulations have been used extensively to simulate equilibrium conditions in planar and porous electrodes.[235] MD simulations have the ability to capture physical phenomena occurring at atomic scale using atomic interaction potentials determined from experimental measurements or from ab initio calculations. However, MD simulations cannot simulate long charging-discharging processes such as cyclic voltammetric or galvanostatic cycling. Similarly, they cannot simulate the multiscale nature of the processes taking place in actual

porous electrodes with realistic separator dimensions due to the excessively large number of atoms or molecules to be simulated. Thus, ab initio, MD simulations, and continuum modeling are complementary modeling methods. For example, the electric-field dependent relative permittivity $\epsilon_r(E)$ can be determined using MD simulations[150] (Figure 4) and used as a continuum property in continuum models.[146] However, more effort needs to be made to connect MD simulations results to the different input parameters of the previously discussed continuum models. For example, MD simulations could be used to determine (i) the Stern layer thickness currently assumed to be identical to the ion radius, (ii) the effective diameter of solvated and unsolvated ions, and (iii) their diffusion coefficient in the electrolyte. MD simulations could also inform potential refinements of continuum models to account for (a) partial ion solvation near the electrode surface, (b) complete ion desolvation as ions enter narrow pores,[236] and (c) the overscreening effect due to the formation of multiple layers of ions with alternating valency near the electrode surface. Note that several studies[237–240] have directly compared the predictions of MD simulations and continuum models, in particular for EDLs in ionic liquids. These studies have mainly focused on assessing the applicability of the continuum models.[238–240] Cagle et al.[237] coupled the two modeling approaches by retrieving the ion mobilities, effective Stern layer thicknesses, and inter-electrode spacing for a PNP model with Stern layer from MD simulations. The effective Stern layer thicknesses were fitted so that both models predicted the same surface charge density, while the inter-electrode spacing was based on the distance between the concentration peaks for the cations and anions adjacent to their respective counter electrodes.[237] The authors concluded that the PNP model provided a reasonable approximation of the ion concentration profiles and the temporal variation of the surface charge density, although it could not capture the non-monotonic spatial variation of ion concentrations.[237] The classical PNP model was considered applicable because the ion concentrations never reached the steric limit corresponding to face-centered cubic packing.[237]

Finally, the mathematical framework present in this paper can be extended to pseudocapacitive electrodes featuring redox reactions with or without ion intercalation. It can also be developed for hybrid pseudocapacitors to improve their performance by choosing the optimum combination of pseudocapacitive electrode materials and morphology, carbon electrode morphology, and electrolyte.[241,242] Similarly, the thermal behaviors of pseudocapacitors can be modeled to provide guidelines for thermal management and avoid premature performance degradation and potential hazards.

Acknowledgment

References

1. E. Frackowiak and F. Béguin, Carbon materials for the electrochemical storage of energy in capacitors, *Carbon*, **39**(6), 937 (2001).
2. US Department of Energy, Basic Research Needs for Electrical Energy Storage: Report of the Basic Energy Sciences Workshop on Electrical Energy Storage, www.osti.gov/accomplishments/documents/fullText/ACC0330.pdf (April 2-4, 2007).
3. A. Burke, Ultracapacitors: why, how, and where is the technology, *Journal of Power Sources*, **91**(1), 37 (2000).
4. L. L. Zhang and X. S. Zhao, Carbon-based materials as supercapacitor electrodes, *Chemical Society Reviews*, **38**(9), 2520 (2009).
5. A. S. Arico, P. Bruce, B. Scrosati, J. M. Tarascon, and W. V. Schalkwijk, Nanostructured materials for advanced energy conversion and storage devices, *Nature Materials*, **4**(5), 366 (2005).
6. E. Frackowiak, Carbon materials for supercapacitor application, *Physical Chemistry Chemical Physics*, **9**(15), 1774 (2007).
7. Y. Zhang, H. Feng, X. Wu, L. Wang, A. Zhang, T. Xia, H. Dong, X. Li, and L. Zhang, Progress of electrochemical capacitor electrode materials: A review, *International Journal of Hydrogen Energy*, **34**(11), 4889 (2009).
8. P. Simon and Y. Gogotsi, Materials for electrochemical capacitors, *Nature Materials*, **7**(11), 845 (2008).
9. G. Gryglewicz, J. Machnikowski, E. Lorenc-Grabowska, G. Lota, and E. Frackowiak, Effect of pore size distribution of coal-based activated carbons on double layer capacitance, *Electrochimica Acta*, **50**(5), 1197 (2005).
10. C. Vix-Guterl, E. Frackowiak, K. Jurewicz, M. Friebe, J. Parmentier, and F. Béguin, Electrochemical energy storage in ordered porous carbon materials, *Carbon*, **43**(6), 1293 (2005).
11. A. B. Fuertes, G. Lota, T. A. Centeno, and E. Frackowiak, Templated mesoporous carbons for supercapacitor application, *Electrochimica Acta*, **50**(14), 2799 (2005).
12. H. Shi, Activated carbons and double layer capacitance, *Electrochimica Acta*, **41**(10), 1633 (1996).
13. D. Qu and H. Shi, Studies of activated carbons used in double-layer capacitors, *Journal of Power Sources*, **74**(1), 99 (1998).
14. O. Barbieri, M. Hahn, A. Herzog, and R. Kötz, Capacitance limits of high surface area activated carbons for double layer capacitors, *Carbon*, **43**(6), 1303 (2005).
15. P. Liu, M. Verbrugge, and S. Soukiazian, Influence of temperature and electrolyte on the performance of activated-carbon supercapacitors, *Journal of Power Sources*, **156**(2), 712 (2006).
16. V. V. N. Obreja, On the performance of supercapacitors with electrodes based on carbon nanotubes and carbon activated material - A review, *Physica E: Low-dimensional Systems and Nanostructures*, **40**(7), 2596 (2008).
17. E. Frackowiak, K. Metenier, V. Bertagna, and F. Béguin, Supercapacitor electrodes from multiwalled carbon nanotubes, *Applied Physics Letters*, **77**(15), 2421 (2000).
18. E. Frackowiak, Electrochemical storage of energy in carbon nanotubes and nanostructured carbons, *Carbon*, **40**(10), 1774 (2002).
19. K. Jurewicz, S. Delpeux, V. Bertagna, F. Béguin, and E. Frackowiak, Supercapacitors from nanotubes/polypyrrole composites, *Chemical Physics Letters*, **347**(1-3), 36 (2001).
20. K. H. An, W. S. Kim, Y. S. Park, Y. C. Choi, S. M. Lee, D. C. Chung, D. J. Bae, S. C. Lim, and Y. H. Lee, Supercapacitors using single-walled carbon nanotube electrodes, *Advanced Materials*, **13**(7), 497 (2001).
21. K. H. An, W. S. Kim, Y. S. Park, J. M. Moon, D. J. Bae, S. C. Lim, Y. S. Lee, and Y. H. Lee, Electrochemical properties of high-power supercapacitors using single-walled carbon nanotube electrodes, *Advanced Functional Materials*, **11**(5), 387 (2001).
22. K. H. An, K. K. Jeon, J. K. Heo, S. C. Lim, D. J. Bae, and Y. H. Lee, High-capacitance supercapacitor using a nanocomposite electrode of single-walled carbon nanotube and polypyrrole, *Journal of The Electrochemical Society*, **149**(8), 1058 (2002).
23. M. Hughes, G. Z. Chen, M. S. P. Shaffer, D. J. Fray, and A. H. Windle, Electrochemical capacitance of a nanoporous composite of carbon nanotubes and polypyrrole, *Chemistry of Materials*, **14**(4), 1610 (2002).
24. J. H. Chen, W. Z. Li, D. Z. Wang, S. X. Yang, J. G. Wen, and Z. F. Ren, Electrochemical characterization of carbon nanotubes as electrode in electrochemical double-layer capacitors, *Carbon*, **40**(8), 1193 (2002).
25. Q. Xiao and X. Zhou, The study of multiwalled carbon nanotube deposited with conducting polymer for supercapacitor, *Electrochimica Acta*, **48**(5), 575 (2003).
26. D. N. Futaba, K. Hata, T. Yamada, T. Hiraoka, Y. Hayamizu, Y. Kakudate, O. Tanaike, H. Hatori, M. Yumura, and S. Iijima, Shape-engineerable and highly densely packed single-walled carbon nanotubes and their application as supercapacitor electrodes, *Nature Materials*, **5**(12), 987 (2006).
27. C. Yu, C. Masarapu, J. Rong, B. Wei, and H. Jiang, Stretchable supercapacitors based on buckled single-walled carbon-nanotube macrofilms, *Advanced Materials*, **21**(47), 4793 (2009).
28. Y. Honda, T. Ono, M. Takeshige, N. Morihara, H. Shiozaki, T. Kitamura, K. Yoshikawa, M. Morita, M. Yamagata, and M. Ishikawa, Effect of MWCNT bundle structure on electric double-layer capacitor performance, *Electrochemical and Solid-State Letters*, **12**(3), 45 (2009).
29. A. B. Fuertes, F. Pico, and J. M. Rojo, Influence of pore structure on electric double-layer capacitance of template mesoporous carbons, *Journal of Power Sources*, **133**(2), 329 (2004).
30. M. Sevilla, S. Alvarez, T. A. Centeno, A. B. Fuertes, and F. Stoeckli, Performance of templated mesoporous carbons in supercapacitors, *Electrochimica Acta*, **52**(9), 3207 (2007).
31. J. Li, X. Wang, Q. Huang, S. Gamboa, and P. J. Sebastian, Studies on preparation and performances of carbon aerogel electrodes for the application of supercapacitor, *Journal of Power Sources*, **158**(1), 784 (2006).
32. T. Bordjiba, M. Mohamedi, and L. H. Dao, New class of carbon-nanotube aerogel electrodes for electrochemical power sources, *Advanced Materials*, **20**(4), 815 (2008).
33. C. Liu, Z. Yu, D. Neff, A. Zhamu, and B. Z. Jang, Graphene-based supercapacitor with an ultrahigh energy density, *Nano Letters*, **10**(12), 4863 (2010).
34. T. Y. Kim, H. W. Lee, M. Stoller, D. R. Dreyer, C. W. Bielawski, R. S. Ruoff, and K. S. Suh, High-performance supercapacitors based on poly(ionic liquid)-modified graphene electrodes, *ACS Nano*, **5**(1), 436 (2011).
35. M. F. El-Kady, V. Strong, S. Dubin, and R. B. Kaner, Laser scribing of high-performance and flexible graphene-based electrochemical capacitors, *Science*, **335**(6074), 1326 (2012).
36. B. E. Conway, *Electrochemical Supercapacitors: Scientific Fundamentals and Technological Applications* Kluwer Academic/Plenum Publishers, New York, NY, 1999.
37. R. Kotz and M. Carlen, Principles and applications of electrochemical capacitors, *Electrochimica Acta*, **45**(15), 2483 (2000).

38. H. L. F. von Helmholtz, Studien über electrische Grenzschichten, *Annalen der Physik*, **243**(7), 337 (1879).

39. J. H. Masliyah and S. Bhattacharjee, *Electrokinetic and Colloid Transport Phenomena* John Wiley & Sons, Hoboken, NJ, 2006.

40. V. Bagotsky, *Fundamentals of Electrochemistry* John Wiley & Sons, Hoboken, NJ, 2006.

41. A. J. Bard and L. R. Faulkner, *Electrochemical Methods: Fundamentals and Applications* John Wiley & Sons, New York, NY, 2001.

42. G. Gouy, Sur la constitution de la charge électrique à la surface d'un électrolyte, *Journal of Physics*, **9**(1), 457 (1910).

43. D. L. Chapman, A contribution to the theory of electrocapillarity, *Philosophical Magazine, Series 6*, **25**(148), 475 (1913).

44. O. Stern, Zur theorie der elektrolytischen doppelschicht, *Zeitschrift für Elektrochemie und Angewandte Physikalische Chemie*, **30**, 508 (1924).

45. D. C. Grahame, The electrical double layer and the theory of electrocapillarity, *Chemical Reviews*, **41**(3), 441 (1947).

46. C. P. Smith and H. S. White, Theory of the voltammetric response of electrodes of submicron dimensions. Violation of electroneutrality in the presence of excess supporting electrolyte, *Analytical Chemistry*, **65**(23), 3343 (1993).

47. K. B. Oldham and A. M. Bond, How valid is the electroneutrality approximation in the theory of steady-state voltammetry?, *Journal of Electroanalytical Chemistry*, **508**(1-2), 28 (2001).

48. J. S. Newman and K. E. Thomas-Alyea, *Electrochemical Systems*, 3rd Edition, John Wiley & Sons, Hoboken, N.J., 2004.

49. V. S. Bagotsky, *Fundamentals of Electrochemistry*, 2nd Edition, John Wiley & Sons, Hoboken, NJ, 2006.

50. M. Arulepp, L. Permann, J. Leis, A. Perkson, K. Rumma, A. Janes, and E. Lust, Influence of the solvent properties on the characteristics of a double layer capacitor, *Journal of Power Sources*, **133**(2), 320 (2004).

51. J. Bisquert, *Nanostructured Energy Devices: Equilibrium Concepts and Kinetics*, CRC Press, Boca Raton, FL, 2015.

52. T. Pandolfo, V. Ruiz, S. Sivakkumar, and J. Nerkar, General properties of electrochemical capacitors, in: F. Béguin and E. Frackowiak (Eds.), *Supercapacitors: Materials, Systems, and Applications*, Wiley-VCH Verlag, Weinheim, Germany, 2013, Ch. 2, pp. 69–109.

53. B. E. Conway and W. G. Pell, Power limitations of supercapacitor operation associated with resistance and capacitance distribution in porous electrode devices, *Journal of Power Sources*, **105**(2), 169 (2002).

54. S. Yoon, J. H. Jang, B. H. Ka, and S. M. Oh, Complex capacitance analysis on rate capability of electric-double layer capacitor (EDLC) electrodes of different thickness, *Electrochimica Acta*, **50**(11), 2255 (2005).

55. O. Bohlen, J. Kowal, and D. Sauer, Ageing behavior of electrochemical double layer capacitors: Part I. Experimental study and aging model, *Journal of Power Sources*, **172**(1), 468 (2007).

56. S. Yoon, C. W. Lee, and S. M. Oh, Characterization of equivalent series resistance of electric double-layer capacitor electrodes using transient analysis, *Journal of Power Sources*, **195**(13), 4391 (2010).

57. M. Kaus, J. Kowa, and D. U. Sauer, Modelling the effects of charge redistribution during self-discharge of supercapacitors, *Electrochimica Acta*, **55**(25), 7516 (2010).

58. R. Spyker and R. Nelms, Classical equivalent circuit parameters for a double-layer capacitor, *IEEE Transactions on Aerospace and Electronic Systems*, **36**(3), 829 (2000).

59. L. Zubieta and R. Bonert, Characterization of double-layer capacitors for power electronics applications, *Industry Applications, IEEE Transactions on*, **36**(1), 199 (2000).

60. R. de Levie, On porous electrodes in electrolyte solutions—IV, *Electrochimica Acta* **9**(9) 1231 (1964).

61. T. Funaki, Evaluating energy storage efficiency by modeling the voltage and temperature dependency in EDLC electrical characteristics, *IEEE Transactions on Power Electronics*, **25**(5), 1231 (2010).

62. J. F. Rubinson and Y. P. Kayinamura, Charge transport in conducting polymers: insights from impedance spectroscopy, *Chemical Society Reviews*, **38**(12), 3339 (2009).

63. M. Z. Bazant, K. Thornton, and A. Ajdari, Diffuse-charge dynamics in electrochemical systems, *Physical Review E* **70**(2) 021506 (2004).

64. L. H. Olesen, M. Z. Bazant, and H. Bruus, Strongly nonlinear dynamics of electrolytes in large ac voltages, *Physical Review E* **82**(1) 011501 (2010).

65. K. T. Chu and M. Z. Bazant, Nonlinear electrochemical relaxation around conductors, *Physical Review E* **74**(1) 011501 (2006).

66. I. Rubinstein, E. Sabatani, and J. Rishpon, Electrochemical impedance analysis of polyaniline films on electrodes, *Journal of The Electrochemical Society*, **134**(12), 3078 (1987).

67. J. Tanguy, N. Mermilliod, and M. Hoclet, Capacitive charge and noncapacitive charge in conducting polymer electrodes, *Journal of The Electrochemical Society*, **134**(4), 795 (1987).

68. M. Kalaji and L. M. Peter, Optical and electrical A.C. response of polyaniline films, *Journal of The Chemical Society, Faraday Transactions*, **87**(6), 853 (1991).

69. J. Bobacka, A. Lewenstam, and A. Ivaska, Electrochemical impedance spectroscopy of oxidized poly(3,4-ethylenedioxythiophene) film electrodes in aqueous solutions, *Journal of Electroanalytical Chemistry*, **489**(1-2), 17 (2000).

70. W. Sun and X. Chen, Preparation and characterization of polypyrrole films for three-dimensional micro supercapacitor, *Journal of Power Sources*, **193**(2), 924 (2009).

71. A. M. Johnson and J. Newman, Desalting by means of porous carbon electrodes, *Journal of The Electrochemical Society*, **118**(3), 510 (1971).

72. B. Pillay and J. Newman, The influence of side reactions on the performance of electrochemical double-layer capacitors, *Journal of The Electrochemical Society*, **143**(6), 1806 (1996).

73. I. J. Ong and J. Newman, Double-layer capacitance in a dual lithium ion insertion cell, *Journal of The Electrochemical Society*, **146**(12), 4360 (1999).

74. V. Srinivasan and J. W. Weidner, Mathematical modeling of electrochemical capacitors, *Journal of The Electrochemical Society*, **146**(5), 1650 (1999).

75. C. Lin, J. A. Ritter, B. N. Popov, and R. E. White, A mathematical model of an electrochemical capacitor with double-layer and faradaic processes, *Journal of The Electrochemical Society*, **146**(9), 3168 (1999).

76. C. Lin, B. N. Popov, and H. J. Ploehn, Modeling the effects of electrode composition and pore structure on the performance of electrochemical capacitors, *Journal of The Electrochemical Society*, **149**(2), 167 (2002).

77. D. Dunn and J. Newman, Predictions of specific energies and specific powers of double-layer capacitors using a simplified model, *Journal of The Electrochemical Society*, **147**(3), 820 (2000).

78. H. Kim and B. N. Popov, A mathematical model of oxide, carbon composite electrode for supercapacitors, *Journal of the Electrochemical Society*, **150**(9), 1153 (2003).

79. G. Sikha, R. E. White, and B. N. Popov, A mathematical model for a lithium-ion battery/electrochemical capacitor hybrid system, *Journal of The Electrochemical Society*, **152**(8), 1682 (2005).

80. M. W. Verbrugge and P. Liu, Microstructural analysis and mathematical modeling of electric double-layer supercapacitors, *Journal of The Electrochemical Society*, **152**(5), 79 (2005).

81. S. Kazaryan, S. Razumov, S. Litvinenko, G. Kharisov, and V. Kogan, Mathematical model of heterogeneous electrochemical capacitors and calculation of their parameters, *Journal of The Electrochemical Society*, **153**(9), 1655 (2006).

82. S. K. Griffiths and R. H. Nilson, Optimum interparticle porosity for charge storage in a packed bed of nanoporous particles, *Journal of The Electrochemical Society*, **157**(4), 469 (2010).

83. J. R. Miller, Electrochemical capacitor thermal management issues at high-rate cycling, *Electrochimica Acta*, **52**(4), 1703 (2006).

84. P. Liu, M. Verbrugge, and S. Soukiazian, Influence of temperature and electrolyte on the performance of activated-carbon supercapacitors, *Journal of Power Sources*, **156**(2), 712 (2006).

85. H. Michel, Temperature and dynamics problems of ultracapacitors in stationary and mobile applications, *Journal of Power Sources*, **154**(2), 556 (2006).

86. F. Rafik, H. Gualous, R. Gallay, A. Crausaz, and A. Berthon, Frequency, thermal and voltage supercapacitor characterization and modeling, *Journal of Power Sources*, **165**(2), 928 (2007).

87. A. Lewandowski and M. Galinski, Practical and theoretical limits for electrochemical double-layer capacitors, *Journal of Power Sources*, **173**(2), 822 (2007).

88. M. Al Sakka, H. Gualous, J. Van Mierlo, and H. Culcu, Thermal modeling and heat management of supercapacitor modules for vehicle applications, *Journal of Power Sources*, **194**(2), 581 (2009).

89. H. Gualous, H. Louahlia-Gualous, R. Gallay, and A. Miraoui, Supercapacitor thermal modeling and characterization in transient state for industrial applications, *IEEE Transactions on Industry Applications*, **45**(3), 1035 (2009).

90. P. Guillemet, Y. Scudeller, and T. Brousse, Multi-level reduced-order thermal modeling of electrochemical capacitors, *Journal of Power Sources*, **157**(1), 630 (2006).

91. O. Bohlen, J. Kowal, and D. Sauer, Ageing behavior of electrochemical double layer capacitors: Part II. Lifetime simulation model for dynamic applications, *Journal of Power Sources*, **173**(1), 626 (2007).

92. J. Schiffer, D. Linzen, and D. U. Sauer, Heat generation in double layer capacitors, *Journal of Power Sources*, **160**(1), 765 (2006).

93. H. Wang and L. Pilon, Accurate simulation of electric double layer capacitance for ultramicroelectrodes, *Journal of Physical Chemistry C*, **115**(33), 16711 (2011).

94. A. A. Kornyshev, Double-layer in ionic liquids: Paradigm change?, *Journal of Physical Chemistry B*, **111**(20), 5545 (2007).

95. M. Z. Bazant, M. S. Kilic, B. D. Storey, and A. Ajdari, Towards an understanding of induced-charge electrokinetics at large applied voltages in concentrated solutions, *Advances in Colloid and Interface Science*, **152**(1-2), 48 (2009).

96. J. J. Bikerman, Structure and capacity of electrical double layer, *Philosophical Magazine*, **33**(220), 384 (1942).

97. I. Borukhov, D. Andelman, and H. Orland, Steric effects in electrolytes: A modified Poisson-Boltzmann equation, *Physical Review Letters*, **79**(3), 435 (1997).

98. I. Borukhov, D. Andelman, and H. Orland, Adsorption of large ions from an electrolyte solution: a modified Poisson-Boltzmann equation, *Electrochimica Acta*, **46**(2-3), 221 (2000).

99. M. S. Kilic, M. Z. Bazant, and A. Ajdari, Steric effects in the dynamics of electrolytes at large applied voltages. I. Double-layer charging, *Physical Review E*, **75**(2), 021502 (2007).

100. C. W. Outhwaite and L. B. Bhuiyan, An improved modified Poisson-Boltzmann equation in electric-double-layer theory, *Journal of the Chemical Society. Faraday Transactions II*, **79**, 707 (1983).

101. V. Vlachy, Ionic effects beyond Poisson-Boltzmann theory, *Annual Review of Physical Chemistry*, **50**, 145 (1999).

102. J. J. López-García, M. J. Aranda-Rascón, and J. Horno, Electrical double layer around a spherical colloid particle: The excluded volume effect, *Journal of Colloid and Interface Science*, **316**(1), 196 (2007).

103. P. M. Biesheuvel and J. Lyklema, Sedimentation-diffusion equilibrium of binary mixtures of charged colloids including volume effects, *Journal of Physics: Condensed Matter*, **17**(41), 6337 (2005).

104. P. M. Biesheuvel and M. van Soestbergen, Counterion volume effects in mixed electrical double layers, *Journal of Colloid and Interface Science*, **316**(2), 490 (2007).

105. G. Tresset, Generalized Poisson-Fermi formalism for investigating size correlation effects with multiple ions, *Physical Review E*, **78**(6), 061506 (2008).

106. B. Eisenberg, Interacting ions in biophysics: Real is not ideal, *Biophysical Journal*, **104**(9), 1849 (2013).

107. S. Zhou, Z. Wang, and B. Li, Mean-field description of ionic size effects with nonuniform ionic sizes: A numerical approach, *Physical Review E*, **84**(2), 021901 (2011).

108. I. Borukhov, D. Andelman, and H. Orland, Steric effects in electrolytes: A modified Poisson-Boltzmann equation, *Physical Review Letters*, **79**(3), 435 (1997).

109. I. Borukhov, D. Andelman, and H. Orland, Adsorption of large ions from an electrolyte solution: a modified Poisson-Boltzmann equation, *Electrochimica Acta*, **46**(2-3), 221 (2000).

110. A. R. J. Silalahi, A. H. Boschitsch, R. C. Harris, and M. O. Fenley, Comparing the predictions of the nonlinear Poisson-Boltzmann equation and the ion size-modified Poisson-Boltzmann equation for a low-dielectric charged spherical cavity in an aqueous salt solution, *Journal of Chemical Theory and Computation*, **6**(12), 3631 (2010).

111. V. B. Chu, Y. Bai, J. Lipfert, D. Herschlag, and S. Doniach, Evaluation of ion binding to DNA duplexes using a size-modified Poisson-Boltzmann theory, *Biophysical Journal*, **93**(9), 3202 (2007).

112. P. Grochowski and J. Trylska, Continuum molecular electrostatics, salt effects, and counterion binding - A review of the Poisson-Boltzmann theory and its modifications, *Biopolymers*, **89**(2), 93 (2008).

113. P. M. Biesheuvel, F. A. M. Leermakers, and M. A. C. Stuart, Self-consistent field theory of protein adsorption in a non-Gaussian polyelectrolyte brush, *Physical Review E*, **73**(1), 011802 (2006).

114. P. H. R. Alijó, F. W. Tavares, and E. C. Biscaia Jr., Double layer interaction between charged parallel plates using a modified Poisson-Boltzmann equation to include size effects and ion specificity, *Colloids and Surfaces A*, **412**, 29 (2012).

115. B. Li, Continuum electrostatics for ionic solutions with non-uniform ionic sizes, *Nonlinearity*, **22**(4), 811 (2009).

116. J. Wen, S. Zhou, Z. Xu, and B. Li, Competitive adsorption and ordered packing of counterions near highly charged surfaces: From mean-field theory to Monte Carlo simulations, *Physical Review E*, **85**(4), 041406 (2012).

117. J. J. López-García, M. J. Aranda-Rascón, and J. Horno, Excluded volume effect on the electrophoretic mobility of colloidal particles, *Journal of Colloid and Interface Science*, **323**(1), 146 (2008).

118. M. J. Aranda-Rascón, C. Grosse, J. J. López-García, and J. Horno, Electrokinetics of suspended charged particles taking into account the excluded volume effect, *Journal of Colloid and Interface Science*, **335**(2), 250 (2009).

119. J. J. López-García, J. Horno, and C. Grosse, Equilibrium properties of charged spherical colloidal particles suspended in aqueous electrolytes: Finite ion size and effective ion permittivity effects, *Journal of Colloid and Interface Science*, **380**(1), 213 (2012).

120. J. J. López-García and J. Horno, Poisson-Boltzmann description of the electrical double layer including ion size effects, *Langmuir*, **27**(23), 13970 (2011).

121. J. J. López-García, M. J. Aranda-Rascón, C. Grosse, and J. Horno, Equilibrium electric double layer of charged spherical colloidal particles: Effect of different distances of minimum ion approach to the particle surface, *Journal of Physical Chemistry B*, **114**(22), 7548 (2010).

122. J. J. López-García, M. J. Aranda-Rascón, C. Grosse, and J. Horno, Electrokinetics of charged spherical colloidal particles taking into account the effect of ion size constraints, *Journal of Colloid and Interface Science*, **356**(1), 325 (2011).

123. J. P. Valleau and G. M. Torrie, The electrical double layer. III. modified Gouy-Chapman theory with unequal ion sizes, *Journal of Chemical Physics*, **76**(9), 4623 (1982).

124. J. Yu, G. E. Aguilar-Pineda, A. Antillon, S.-H. Dong, and M. Lozada-Cassou, The effects of unequal ionic sizes for an electrolyte in a charged slit, *Journal of Colloid and Interface Science*, **295**(1), 124 (2006).

125. H. Wang, A. Thiele, and L. Pilon, Simulations of cyclic voltammetry for electric double layers in asymmetric electrolytes: A generalized modified Poisson-Nernst-Planck model, *Journal of Physical Chemistry C* **117**(36), 18286 (2013).

126. E. M. Itskovich, A. A. Kornyshev, and M. A. Vorotyntsev, Electric current across the metal-solid electrolyte interface I. Direct current, current-voltage characteristic, *Physica Status Solidi A*, **39**(1), 229 (1977).

127. A. A. Kornyshev and M. A. Vorotyntsev, Conductivity and space charge phenomena in solid electrolytes with one mobile charge carrier species, a review with original material, *Electrochimica Acta*, **26**(3), 303 (1981).

128. H. Wang and L. Pilon, Mesoscale modeling of electric double layer capacitors with three-dimensional ordered structures, *Journal of Power Sources*, **221**, 252 (2013).

129. D. Halliday, R. Resnick, and J. Walker, *Fundamentals of Physics*, 9th Edition, John Wiley & Sons, Hoboken, NJ, 2010.

130. F. Booth, The dielectric constant of water and the saturation effect, *Journal of Chemical Physics*, **19**(4), 391 (1951).

131. F. Booth, Errata: The dielectric constant of water and the saturation effect, *Journal of Chemical Physics*, **19**(10), 1327 (1951).

132. A. J. Appleby, Electron transfer reactions with and without ion transfer, in: B. Conway, C. Vayenas, R. White, and M. Gamboa-Adelco (Eds.), *Modern Aspects of Electrochemistry*, No. 38, Kluwer Academic/Plenum Publishers, New York, NY, 2005, pp. 175–301.

133. A. D. Buckingham, Theory of the dielectric constant at high field strengths, *Journal of Chemical Physics*, **25**(3), 428 (1956).

134. I. C. Yeh and M. L. Berkowitz, Dielectric constant of water at high electric fields: Molecular dynamics study, *Journal of Chemical Physics*, **110**(16), 7935 (1999).

135. D. C. Grahame, Effects of dielectric saturation upon the diffuse double layer and the free energy of hydration of ions, *Journal of Chemical Physics*, **18**(7), 903 (1950).

136. H. A. Kotodziej, G. P. Jones, and M. Davies, High field dielectric measurements in water, *Journal of the Chemical Society. Faraday Transactions II*, **175**(71), 269 (1975).

137. J. K. Hyun, C. S. Babu, and T. Ichiye, Apparent local dielectric response around ions in water: A method for its determination and its applications, *Journal of Physical Chemistry*, **99**(14), 5187 (1995).

138. G. Sutmann, Structure formation and dynamics of water in strong external electric fields, *Journal of Electroanalytical Chemistry*, **450**(2), 289 (1998).

139. H. P. Huinink, A. de Keizer, F. A. M. Leermakers, and J. Lyklema, Lattice approach to the dielectric permittivity of water, *Journal of Physical Chemistry*, **100**(23), 9948 (1996).

140. J. Dzubiella and J. P. Hansen, Electric-field-controlled water and ion permeation of a hydrophobic nanopore, *Journal of Chemical Physics*, **122**(23), 234706 (2005).

141. L. Sandberg and O. Edholm, Nonlinear response effects in continuum models of the hydration of ions, *Journal of Chemical Physics*, **116**(7), 2936 (2002).

142. I. Szalai, S. Nagy, and S. Dietrich, Nonlinear dielectric effect of dipolar fluids, *Journal of Chemical Physics*, **131**(15), 154905 (2009).

143. R. L. Fulton, The nonlinear dielectric behavior of water: Comparisons of various approaches to the nonlinear dielectric increment, *Journal of Chemical Physics*, **130**(20), 204503 (2009).

144. Y. Gur, I. Ravina, and A. J. Babchin, On the electrical double layer theory. II. the Poisson-Boltzmann equation including hydration forces, *Journal of Colloid and Interface Science*, **64**(2), 333 (1978).

145. S. Basu and M. M. Sharma, Effect of dielectric saturation on disjoining pressure in thin films of aqueous electrolytes, *Journal of Colloid and Interface Science*, **165**(2), 355 (1994).

146. H. Wang, J. Varghese, and L. Pilon, Simulation of electric double layer capacitors with mesoporous electrodes: Effects of morphology and electrolyte permittivity, *Electrochimica Acta*, **56**(17), 6189 (2011).

147. G. Moumouzias and G. Ritzoulis, Relative permittivities and refractive indexes of propylene carbonate + toluene mixtures: From 283.15 K to 313.15 K, *Journal of Chemical & Engineering Data*, **42**(4), 710 (1997).

148. C. Wohlfarth, *Dielectric Constant of Acetonitrile, Springer Materials - The Landolt-Börnstein Database*, Vol. 17, Springer-Verlag, Berlin, Germany, 2008.

149. C. Wohlfarth, *Refractive Index of Acetonitrile, Springer Materials - The Landolt-Börnstein Database*, Vol. 47, Springer-Verlag, Berlin, Germany, 2008.

150. L. Yang, B. H. Fishbine, A. Migliori, and L. R. Pratt, Dielectric saturation of liquid propylene carbonate in electrical energy storage applications, *Journal of Chemical Physics*, **132**(4), 044701 (2010).

151. M. Sparnaay, *The Electrical Double Layer*, Pergamon Press, Oxford, New York, 1972.

152. P. M. Biesheuvel and J. Lyklema, Volume exclusion effects in the ground-state dominance approximation for polyelectrolyte adsorption on charged interfaces, *The European Physical Journal E*, **16**(4), 353 (2005).

153. D. R. Lide, 90th Edition, CRC Press/Taylor & Francis, Boca Raton, FL, 2010, Ch. 6.

154. J. N. Israelachvili, *Intermolecular and Surface Forces*, 3rd Edition, Academic Press, San Diego, CA, 2010.

155. W. Haynes, T. J. Bruno, and D. R. Lide (Eds.), 94th Edition, CRC Press/Taylor & Francis, Boca Raton, FL, 2013, Ch. 5.

156. A. L. Horvath, *Handbook of Aqueous Electrolyte Solutions: Physical Properties, Estimation, and Correlation Methods*, Ellis Horwood Ltd, Chichester, UK, 1985.

157. K. Nishikawa, Y. Fukunaka, T. Sakka, Y. Ogata, and J. Selman, Measurement of LiClO₄ diffusion coefficient in propylene carbonate by Moiré pattern, *Journal of the Electrochemical Society*, **153**(5), A830 (2006).

158. J. Chmiola, G. Yushin, Y. Gogotsi, C. Portet, P. Simon, and P. L. Taberna, Anomalous increase in carbon capacitance at pore sizes less than 1 nanometer, *Science*, **313**(5794), 1760 (2006).

159. Y.-J. Kim, Y. Masutzawa, S. Ozaki, M. Endo, and M. S. Dresselhaus, PVDC-based carbon material by chemical activation and its application to nonaqueous EDLC, *Journal of The Electrochemical Society*, **151**(6), E199 (2004).

160. C. M. Yang, Y. J. Kim, M. Endo, H. Kanoh, M. Yudasaka, S. Iijima, and K. Kaneko, Nanowindow-regulated specific capacitance of supercapacitor electrodes of single-wall carbon nanohorns, *Journal of the American Chemical Society*, **129**(1), 20 (2007).

161. J. Xu and G. Farrington, A novel electrochemical method for measuring salt diffusion coefficients and ion transference numbers, *Journal of the Electrochemical Society*, **143**(2), L44 (1996).

162. G. Feng, Molecular physics of electrical double layers in electrochemical capacitors, Ph.D Thesis, Department of Mechanical Engineering, Clemson University, Clemson, SC (1995).

163. D. J. Griffiths, *Introduction to Electrodynamics*, 3rd Edition, Prentice Hall, Upper Saddle River, NJ, 1999.

164. J. Varghese, H. Wang, and L. Pilon, Simulating electric double layer capacitance of mesoporous electrodes with cylindrical pores, *Journal of The Electrochemical Society*, **158**(10), 1106 (2011).

165. H. J. Liu, W. J. Cui, L. H. Jin, C. X. Wang, and Y. Y. Xia, Preparation of three-dimensional ordered mesoporous carbon sphere arrays by a two-step templating route and their application for supercapacitors, *Journal of Materials Chemistry*, **19**(22), 3661 (2009).

166. S. W. Woo, K. Dokko, H. Nakano, and K. Kanamura, Preparation of three dimensionally ordered macroporous carbon with mesoporous walls for electric double-layer capacitors, *Journal of Materials Chemistry*, **18**(14), 1674 (2008).

167. H. Wang, J. Fang, and L. Pilon, Scaling laws for carbon-based electric double layer capacitors, *Electrochimica Acta*, **109**, 316 (2013).

168. H. Lu, W. Dai, M. Zheng, N. Li, G. Ji, and J. Cao, Electrochemical capacitive behaviors of ordered mesoporous carbons with controllable pore sizes, *Journal of Power Sources*, **209**, 243 (2012).

169. J. Yan, T. Wei, B. Shao, F. Ma, Z. Fan, M. Zhang, C. Zheng, Y. Shang, W. Qian, and F. Wei, Electrochemical properties of graphene nanosheet/carbon black composites as electrodes for supercapacitors, *Carbon*, **48**(6), 1731 (2010).

170. D. S. Yuan, J. Zeng, J. Chen, and Y. Liu, Highly ordered mesoporous carbon synthesized via in situ template for supercapacitors, *International Journal of Electrochemical Science*, **4**(4), 562 (2009).

171. D. Feng, Y. Lv, Z. Wu, Y. Dou, L. Han, Z. Sun, Y. Xia, G. Zheng, and D. Zhao, Free-standing mesoporous carbon thin films with highly ordered pore architectures for nanodevices, *Journal of the American Chemical Society*, **133**(38), 15148 (2011).

172. K. Jurewicz, C. Vix-Guterl, E. Frackowiak, S. Saadallah, M. Reda, J. Parmentier, J. Patarin, and F. Béguin, Capacitance properties of ordered porous carbon materials prepared by a templating procedure, *Journal of Physics and Chemistry of Solids*, **65**(2-3), 287 (2004).

173. N. Liu, H. Song, and X. Chen, Morphology control of ordered mesoporous carbons by changing HCl concentration, *Journal of Materials Chemistry*, **21**(14), 5345 (2011).

174. J.-W. Lang, X.-B. Yan, X.-Y. Yuan, J. Yang, and Q.-J. Xue, Study on the electrochemical properties of cubic ordered mesoporous carbon for supercapacitors, *Journal of Power Sources*, **196**(23), 10472 (2011).

175. J. Wang, C. Xue, Y. Lv, F. Zhang, B. Tu, and D. Zhao, Kilogram-scale synthesis of ordered mesoporous carbons and their electrochemical performance, *Carbon*, **49**(13), 4580 (2011).

176. J. Zhou, J. He, C. Zhang, T. Wang, D. Sun, Z. Di, and D. Wang, Mesoporous carbon spheres with uniformly penetrating channels and their use as a supercapacitor electrode material, *Materials Characterization*, **61**(1), 31 (2010).

177. F. B. Sillars, S. I. Fletcher, M. Mirzaeian, and P. J. Hall, Effect of activated carbon xerogel pore size on the capacitance performance of ionic liquid electrolytes, *Energy & Environmental Science*, **4**(3), 695 (2011).

178. H. Nishihara, H. Itoi, T. Kogure, P. X. Hou, H. Touhara, F. Okino, and T. Kyotani, Investigation of the ion storage/transfer behavior in an electrical double-layer capacitor by using ordered microporous carbons as model materials, *Chemistry - A European Journal*, **15**(21), 5355 (2009).

179. Y. Lv, L. Gan, M. Liu, W. Xiong, Z. Xu, D. Zhu, and D. S. Wright, A self-template synthesis of hierarchical porous carbon foams based on banana peel for supercapacitor electrodes, *Journal of Power Sources*, **209**, 152 (2012).

180. Y. Lv, F. Zhang, Y. Dou, Y. Zhai, J. Wang, H. Liu, Y. Xia, B. Tu, and D. Zhao, A comprehensive study on KOH activation of ordered mesoporous carbons and their supercapacitor application, *Journal of Materials Chemistry*, **22**(1), 93 (2012).

181. L. Jiang, J. Yan, L. Hao, R. Xue, G. Sun, and B. Yi, High rate performance activated carbons prepared from ginkgo shells for electrochemical supercapacitors, *Carbon*, **56**, 146 (2013).

182. F. Li, M. Morris, and K.-Y. Chan, Electrochemical capacitance and ionic transport in the mesoporous shell of a hierarchical porous core–shell carbon structure, *Journal of Materials Chemistry*, **21**(24), 8880 (2011).

183. Y. Gogotsi, A. Nikitin, H. Ye, W. Zhou, J. E. Fischer, B. Yi, H. C. Foley, and M. W. Barsoum, Nanoporous carbide-derived carbon with tunable pore size, *Nature Materials*, **2**(9), 591 (2003).

184. M. S. Kilic, M. Z. Bazant, and A. Ajdari, Steric effects in the dynamics of electrolytes at large applied voltages. II. Modified Poisson-Nernst-Planck equations, *Physical Review E*, **75**(2), 021503 (2007).

185. G. M. Goldin, A. M. Colclasure, A. H. Wiedemann, and R. J. Kee, Three-dimensional particle-resolved models of Li-ion batteries to assist the evaluation of empirical parameters in one-dimensional models, *Electrochimica Acta*, **64**, 118 (2012).

186. A. H. Wiedemann, G. M. Goldin, S. A. Barnett, H. Zhu, and R. J. Kee, Effects of three-dimensional cathode microstructure on the performance of lithium-ion battery cathodes, *Electrochimica Acta*, **88**, 580 (2013).

187. A. Lasia, Electrochemical impedance spectroscopy and its applications, in: B. E. Conway, J. O. M. Bockris, and R. E. White (Eds.), *Modern Aspects of Electrochemistry*, No. 32, Kluwer Academic Publishers, New York, NY, 2002, Ch. 2, pp. 143–248.

188. M. E. Orazem and B. Tribollet, *Electrochemical Impedance Spectroscopy*, John Wiley & Sons, Hoboken, New Jersey, 2008.

189. X. Z. Yuan, C. Song, H. Wang, and J. Zhang, *Electrochemical Impedance Spectroscopy in PEM Fuel Cells: Fundamentals and Applications*, Springer-Verlag, London, UK, 2010.

190. D. Pech, M. Brunet, H. Durou, P. Huang, V. Mochalin, Y. Gogotsi, P. L. Taberna, and P. Simon, Ultrahigh-power micrometer-sized supercapacitors based on onion-like carbon, *Nature Nanotechnology*, **5**(9), 651 (2010).

191. H. Itoi, H. Nishihara, T. Kogure, and T. Kyotani, Three-dimensionally arrayed and mutually connected 1.2-nm nanopores for high-performance electric double layer capacitor, *Journal of the American Chemical Society*, **133**(5), 1165 (2011).

192. A. d'Entremont and L. Pilon, First-principles thermal modeling of electric double layer capacitors under constant-current cycling, *Journal of Power Sources*, **246**, 887 (2014).

193. L. L. Zhang, R. Zhou, and X. S. Zhao, Graphene-based materials as supercapacitor electrodes, *Journal of Materials Chemistry*, **20**(29), 5983 (2010).

194. J. Sanchez-Gonzalez, F. Stoeckli, and T. A. Centeno, The role of the electric conductivity of carbons in the electrochemical capacitor performance, *Journal of Electroanalytical Chemistry*, **657**(1-2), 176 (2011).

195. H. Wang and L. Pilon, Physical interpretation of cyclic voltammetry for measuring electric double layer capacitances, *Electrochimica Acta*, **64**, 130 (2012).

196. P. L. Taberna, P. Simon, and J. F. Fauvarque, Electrochemical characteristics and impedance spectroscopy studies of carbon-carbon supercapacitors, *Journal of The Electrochemical Society*, **150**(3), 292 (2003).

197. E. Barsoukov and J. R. Macdonald, *Impedance Spectroscopy: Theory, Experiment, and Applications*, 2nd Edition, John Wiley & Sons, Hoboken, New Jersey, 2005.

198. H. Wang and L. Pilon, Reply to comments on "Intrinsic limitations of impedance measurements in determining electric double layer capacitances" by H. Wang and L. Pilon [Electrochimica Acta 63 (2012) 55], *Electrochimica Acta*, **76**(0), 529 (2012).

199. H. Wang, H. S. Casalongue, Y. Liang, and H. Dai, Ni(OH)$_2$ nanoplates grown on graphene as advanced electrochemical pseudocapacitor materials,, *Journal of the American Chemical Society*, **132**(21), 7472 (2010).

200. L.-Q. Mai, F. Yang, Y.-L. Zhao, X. Xu, L. Xu, and Y.-Z. Luo, Hierarchical MnMoO$_4$/CoMoO$_4$ heterostructured nanowires with enhanced supercapacitor performance, *Nature Communications*, **2**(381), 1 (2011).

201. J. Feng, X. Sun, C. Wu, L. Peng, C. Lin, S. Hu, J. Yang, and Y. Xie, Metallic few-layered VS$_2$ ultrathin nanosheets: High two-dimensional conductivity for in-plane supercapacitors, *Journal of the American Chemical Society*, **133**(44), 17832 (2011).

202. B. G. Choi, J. Hong, W. H. Hong, P. T. Hammond, and H. Park, Facilitated ion transport in all-solid-state flexible supercapacitors, *ACS Nano*, **5**(9), 7205 (2011).

203. S. K. Meher and G. R. Rao, Ultralayered Co$_3$O$_4$ for high-performance supercapacitor applications, *Journal of Physical Chemistry C*, **115**(31), 15646 (2011).

204. R. B. Rakhi, D. Cha, W. Chen, and H. N. Alshareef, Electrochemical energy storage devices using electrodes incorporating carbon nanocoils and metal oxides nanoparticles, *Journal of Physical Chemistry C*, **115**(29), 14392 (2011).

205. R. Mysyk, E. Raymundo-Pinero, J. Pernak, and F. Béguin, Confinement of symmetric tetraalkylammonium ions in nanoporous carbon electrodes of electric double-layer capacitors, *Journal of Physical Chemistry C*, **113**(30), 13443 (2009).

206. R. Mysyk, E. Raymundo-Pinero, and F. Béguin, Saturation of subnanometer pores in an electric double-layer capacitor, *Electrochemistry Communications*, **11**(3), 554 (2009).

207. H. A. Andreas and B. E. Conway, Examination of the double-layer capacitance of an high specific-area C-cloth electrode as titrated from acidic to alkaline pHs, *Electrochimica Acta*, **51**(28), 6510 (2006).

208. W. Li, D. Chen, Z. Li, Y. Shi, Y. Wan, J. Huang, J. Yang, D. Zhao, and Z. Jiang, Nitrogen enriched mesoporous carbon spheres obtained by a facile method and its application for electrochemical capacitor, *Electrochemistry Communications*, **9**(4), 569 (2007).

209. B. Xu, F. Wu, R. Chen, G. Cao, S. Chen, Z. Zhou, and Y. Yang, Highly mesoporous and high capacitance carbon: A high surface area electrode material for EDLCs with various electrolytes, *Electrochemistry Communications*, **10**(5), 795 (2008).

210. W. G. Pell, B. E. Conway, and N. Marincic, Analysis of non-uniform charge/discharge and rate effects in porous carbon capacitors containing sub-optimal electrolyte concentrations, *Journal of Electroanalytical Chemistry*, **491**(1-2), 9 (2000).

211. M. Inagaki, H. Konno, and O. Tanaike, Carbon materials for electrochemical capacitors, *Journal of Power Sources*, **195**(24), 7880 (2010).

212. F. Béguin, K. Szostak, G. Lota, and E. Frackowiak, A self-supporting electrode for supercapacitors prepared by one-step pyrolysis of carbon nanotube/polyacrylonitrile blend, *Advanced Materials*, **17**(19), 2380 (2005).

213. D. Hulicova, J. Yamashita, Y. Soneda, H. Hatori, and M. Kodama, Supercapacitors prepared from melamine-based carbon, *Chemistry of Materials*, **17**(5), 1241 (2005).

214. T. Wang, A. Kiebele, J. Ma, S. Mhaisalkar, and G. Gruner, Charge transfer between polyaniline and carbon nanotubes supercapacitors: Improving both energy and power densities, *Journal of The Electrochemical Society*, **158**(1), A1 (2011).

215. M. Kawaguchi, A. Itoh, S. Yagi, and H. Oda, Preparation and characterization of carbonaceous materials containing nitrogen as electrochemical capacitor, *Journal of Power Sources*, **172**(1), 481 (2007).

216. M. Seredych, D. Hulicova-Jurcakova, G. Q. Lu, and T. J. Bandosz, Surface functional groups of carbons and the effects of their chemical character, density and accessibility to ions on electrochemical performance, *Carbon*, **46**(11), 1475 (2008).

217. H. Konno, H. Onishi, N. Yoshizawa, and K. Azumi, MgO-templated nitrogen-containing carbons derived from different organic compounds for capacitor electrodes, *Journal of Power Sources*, **195**(2), 667 (2010).

218. A. L. d'Entremont and L. Pilon, Thermal effects of asymmetric electrolytes in electric double layer capacitors, *Journal of Power Sources*, **273**, 196 (2015).

219. H. Zhao, Diffuse-charge dynamics of ionic liquids in electrochemical systems, *Physical Review E*, **84**(5), 051504 (2011).

220. C. Pascot, Y. Dandeville, Y. Scudeller, P. Guillemet, and T. Brousse, Calorimetric measurement of the heat generated by a double-layer capacitor cell under cycling, *Thermochimica Acta*, **510**, 53 (2010).

221. Y. Dandeville, P. Guillemet, Y. Scudeller, O. Crosnier, L. Athouel, and T. Brousse, Measuring time-dependent heat profiles of aqueous electrochemical capacitors under cycling, *Thermochimica Acta*, **526**(1-2), 1 (2011).

222. H. Gualous, H. Louahlia, and R. Gallay, Supercapacitor characterization and thermal modeling with reversible and irreversible heat effect, *IEEE Transactions on Power Electronics*, **26**(11), 3402 (2011).

223. F. P. Incropera, D. P. DeWitt, T. L. Bergman, and A. S. Lavine, *Fundamentals of Heat and Mass Transfer*, 6th Edition, John Wiley & Sons, Hoboken, NJ, 2007.

224. C.-J. Chiang, J.-L. Yang, and W.-C. Cheng, Temperature and state-of-charge estimation in ultracapacitors based on extended Kalman filter, *Journal of Power Sources*, **234**, 234 (2013).

225. A. L. d'Entremont and L. Pilon, First-order thermal model of commercial EDLCs, *Applied Thermal Engineering*, **67**(1–2), 439 (2014).
226. D. H. Lee, U. S. Kim, C. B. Shin, B. H. Lee, B. W. Kim, and Y.-H. Kim, Modelling of the thermal behavior of an ultracapacitor for a 42-V automotive electrical system, *Journal of Power Sources*, **175**(1), 664 (2008).
227. K. Wang, L. Zhang, B. Ji, and J. Yuan, The thermal analysis on the stackable supercapacitor, *Energy*, **59**, 440 (2013).
228. W. B. Gu and C. Y. Wang, Thermal-electrochemical modeling of battery systems, *Journal of the Electrochemical Society*, **147**(8), 2910 (2000).
229. P. Biesheuvel, Negative joule heating in ion-exchange membranes, (2014) arXiv:1402.1448.
230. D. Bernardi, E. Pawlikowski, and J. Newman, A general energy balance for battery systems, *Journal of The Electrochemical Society*, **132**(1), 5 (1985).
231. B. J. Kirby, *Micro- and Nanoscale Fluid Mechanics: Transport in Microfluidic Devices*, Cambridge University Press, Cambridge, UK, 2010.
232. A. L. d'Entremont and L. Pilon, Scaling laws for heat generation and temperature oscillations in EDLCs under galvanostatic cycling, *International Journal of Heat and Mass Transfer*, **75**, 637 (2014).
233. S. Whitaker, *The Method of Volume Averaging*, Kluwer Academic Publishers, Netherlands, 1999.
234. R. Palm, H. Kurig, K. Tõnurist, A. Jänes, and E. Lust, Is the mixture of 1-ethyl-3-methylimidazolium tetrafluoroborate and 1-butyl-3-methylimidazolium tetrafluoroborate applicable as electrolyte in electrical double layer capacitors?, *Electrochemistry Communications*, **22**, 203 (2012).
235. R. Burt, G. Birkett, and X. S. Zhao, A review of molecular modeling of electric double layer capacitors, *Physical Chemistry Chemical Physics*, **16**, 6519 (2014).
236. C. Merlet, B. Rotenberg, P. A. Madden, P.-L. Taberna, P. Simon, Y. Gogotsi, and M. Salanne, On the molecular origin of supercapacitance in nanoporous carbon electrodes, *Nature Materials*, **11**(4), 306 (2012).
237. C. Cagle, G. Feng, R. Qiao, J. Huang, B. G. Sumpter, and V. Meunier, Structure and charging kinetics of electrical double layers at large electrode voltages, *Microfluidics and Nanofluidics*, **8**(5), 703 (2010).
238. M. Z. Bazant, B. D. Storey, and A. A. Kornyshev, Double layer in ionic liquids: Overscreening versus crowding, *Physical Review Letters*, **106**(4), 046102 (2011).
239. X. Jiang, J. Huang, H. Zhao, B. G. Sumpter, and R. Qiao, Dynamics of electrical double layer formation in room-temperature ionic liquids under constant-current charging conditions, *Journal of Physics: Condensed Matter*, **26**(28), 284109 (2014).
240. M. V. Fedorov and A. A. Kornyshev, Towards understanding the structure and capacitance of electrical double layer in ionic liquids, *Electrochimica Acta*, **53**(23), 6835 (2008).
241. J. W. Long, D. Bélanger, T. Brousse, W. Sugimoto, M. B. Sassin, and O. Crosnier, Asymmetric electrochemical capacitors–stretching the limits of aqueous electrolytes, *MRS Bulletin*, **36**(7), 513 (2011).
242. Z. Tang, C.-H. Tang, and H. Gong, A high energy density asymmetric supercapacitor from nano-architectured Ni(OH)$_2$/carbon nanotube electrodes, *Advanced Functional Materials*, **22**(6), 1272 (2012).